ZMYND10 functions in a chaperone relay during axonemal dynein assembly

ZMYND10 functions in a chaperone relay during axonemal dynein assembly.

Girish R Mali[1, 10*], Patricia L Yeyati[1*], Seiya Mizuno[2], Daniel O Dodd[1], Peter A Tennant[1], Margaret A Keighren[1], Petra zur Lage[3], Amelia Shoemark[4], Amaya Garcia-Munoz[5], Atsuko Shimada[6], Hiroyuki Takeda[6], Frank Edlich[7], Satoru Takahashi[2, 8], Alexander von Kriegsheim[5, 9], Andrew P Jarman[3] and Pleasantine Mill[1, †]

1. MRC Human Genetics Unit, Institute of Genetics and Molecular Medicine, University of Edinburgh, Edinburgh, UK, EH4 2XU

2. Laboratory Animal Resource Centre, University of Tsukuba, Tsukuba, Japan, 305-8575

3. Centre for Integrative Physiology, University of Edinburgh, Edinburgh, UK, EH8 9XD

4. Division of Molecular and Clinical Medicine, University of Dundee, Dundee, UK, DD1 9SY

5. Systems Biology Ireland, University College Dublin, Dublin, Ireland

6. Department of Biological Sciences, University of Tokyo, Tokyo, Japan, 113-0033

7. Institute for Biochemistry and Molecular Biology, University of Freiburg, Freiburg, Germany, 79104

8. Department of Anatomy and Embryology, Faculty of Medicine, University of Tsukuba, Tsukuba, Japan, 305-8575

9. Edinburgh Cancer Research UK Centre, Institute of Genetics and Molecular Medicine, University of Edinburgh, Edinburgh, UK, EH4 2XU

10. Current address: MRC Laboratory of Molecular Biology, Cambridge, UK, CB2 0QH

* Co-first authors

† Corresponding author: pleasantine.mill@igmm.ed.ac.uk

Abstract:

Molecular chaperones promote the folding and macromolecular assembly of a diverse set of 'client' proteins. How ubiquitous chaperone machineries direct their activities towards specific sets of substrates is unclear. Through the use of mouse genetics, imaging and quantitative proteomics we uncover that ZMYND10 is a novel co-chaperone that confers specificity for the FKBP8-HSP90 chaperone complex towards axonemal dynein clients required for cilia motility. Loss of ZMYND10 perturbs the chaperoning of axonemal dynein heavy chains, triggering broader degradation of dynein motor subunits. We show that pharmacological inhibition of FKBP8 phenocopies dynein motor instability associated with the loss of ZMYND10 in airway cells and that human disease-causing variants of ZMYND10 disrupt its ability to act as an FKBP8-HSP90 co-chaperone. Our study indicates that Primary Ciliary Dyskinesia (PCD), caused by mutations in dynein assembly factors disrupting cytoplasmic pre-assembly of axonemal dynein motors, should be considered a cell-type specific protein-misfolding disease.

Introduction:

Macromolecular motors of the dynein family power the essential beating of motile cilia/flagella. Motile cilia propel sperm cells, generate mucociliary clearance in airways, modulate nodal flow for embryonic left-right patterning and circulate cerebrospinal fluid inside the brain. Force-generating dynein motors are large molecular complexes visible by transmission electron microscopy (TEM), as 'outer' and 'inner dynein arms' (ODA, IDA) spaced at regular intervals along the microtubule axoneme. Each ODA motor consists of catalytic heavy chains (HC), intermediate chains (IC) and light chains (LC); IDAs have a more heterogeneous composition. In mammals, at least 4 ODA and 7 IDA subtypes exist, each containing different HCs (Kollmar, 2016; Wickstead and Gull, 2007). Defective dyneins render cilia immotile, resulting in the severe congenital ciliopathy in humans termed Primary Ciliary Dyskinesia (PCD, OMIM: 242650). Understanding the molecular causes of PCD requires addressing how complex molecular machines like the dyneins get built during cilium biogenesis?

PCD causing mutations are most frequently detected in genes encoding structural ODA subunits such as the intermediate chains (*DNAI1* and *DNAI2*; (Pennarun et al., 1999),(Guichard et al., 2001),(Loges et al., 2008)), or the catalytic heavy chain (*DNAH5*;(Olbrich et al., 2002)), all of which disrupt motor assembly and/or function. Consequently, mutant multiciliated cells form cilia but these fail to move, lacking ODAs by TEM or immunofluorescence.

In addition to these structural subunits of dynein motors, several PCD causing mutations are also found in a newly discovered set of genes, the "dynein axonemal assembly factors" (DNAAFs) whose functions are poorly understood. DNAAFs are proposed to assist Heat Shock Protein (HSP) chaperones to promote subunit folding and cytoplasmic pre-assembly of dynein motors. DNAAFs are presumed to act as cilial-specific co-chaperones based on proteomic identification of interactions with both "client" dynein chains and canonical chaperones. Of the known assembly factors, KTU/DNAAF2 and DYX1C1/DNAAF4 have the most direct biochemical links to HSP90 and HSP70 chaperones, as well as ODA intermediate chain DNAI2 (IC2) (Omran et al., 2008; Tarkar et al., 2013). Additionally, KTU/DNAAF2, PIH1D3/DNAAF6 and SPAG1 share structural domains with key non-catalytic subunits of the R2TP-HSP90 chaperoning complex, PIH1 and TAH1 respectively. R2TP is a well established HSP90 co-chaperone which confers specificity during the assembly of multisubunit enzymes (Pal et al., 2014). DYX1C1/DNAAF4 and LRRC6 each have a CS or p23-like domain(Kott et al., 2012; Tarkar et al., 2013), p23 being a well characterised HSP90 co-chaperone acting during the last steps of the HSP90 chaperone cycle(J. Li and Buchner, 2013). Interactions between LRRC6, DNAAF1/LRRC50 and C21ORF59/Kurly/CFAP298 were also recently reported which, coupled with the phenotypic analysis of *Lrrc6* mutant mice, suggests that these assembly factors may function

together in a late-acting complex (Inaba et al., 2016; Jaffe et al., 2016). The functions of DNAAF3 and DNAAF5/HEATR2 which have no reported links to chaperones, remain elusive (Diggle et al., 2014; Mitchison et al., 2012). Altogether, the current view is that many DNAAFs transiently participate as HSP90 co-chaperones during the macromolecular assembly of dynein motors before they are finally transported into the cilia.

Dynein pre-assembly has been well studied in unicellular eukaryotes such as *Chlamydomonas* and *Paramecium.* For ODAs in *Chlamydomonas*, affinity purification confirmed all three HCs (HCs; α, β, and γ, each of ~500 kDa) and two ICs (IC1, 78 kDa; IC2, 69 kDa) are pre-assembled as a three headed complex and exist in a cytoplasmic pool prior to ciliary entry (Fok et al., 1994; Fowkes and Mitchell, 1998; Qin et al., 2004). This cytoplasmic pre-assembly pathway is highly conserved and exists in all ciliated eukaryotes (Kobayashi and Takeda, 2012). While it is clear that the aforementioned assembly factors aid axonemal dynein pre-assembly, their precise molecular functions within the pre-assembly pathway still remain largely unknown.

Previous studies had established a strong genetic link between loss of ZMYND10, a putative DNAAF, and perturbations in dynein pre-assembly (Cho et al., 2018; Kobayashi et al., 2017; Kurkowiak et al., 2016; Moore et al., 2013; Zariwala et al., 2013), however the molecular role of ZMYND10 as a DNAAF in this process remained unclear. In order to probe the mammalian dynein pre-assembly pathway in greater molecular and cellular detail, we generated *Zmynd10* null mice by CRISPR genome editing. We used different motile ciliated lineages at distinct stages of differentiation from our mammalian mutant model to ascribe a molecular role to ZMYND10 within the dynein pre-assembly pathway.

Our studies implicate a novel chaperone complex comprising of ZMYND10, FKBP8 and HSP90 in the maturation of dynein HC clients and provide novel evidence of the temporally restricted nature of interactions within this chaperone-relay system, later involving LRRC6 likely to promote stable inter-subunit interactions. We postulate that a chaperone-relay system comprising of several discrete chaperone complexes handles the folding and stability of distinct dynein subunits all the while preventing spurious interactions during cytoplasmic pre-assembly.

Results:

Generation of a mammalian PCD model to characterize dynein assembly

We targeted exon 6 of mouse *Zmynd10* to target all predicted protein isoforms, with three guide RNA (gRNA) sequences for CRISPR genome editing and generated several founders with insertion, deletion and inversion mutations (**Figure 1A, Figure 1-figure supplement 1**). Null mutations from the different CRISPR guide RNAs gave identical phenotypes, confirming the phenotypes are due to loss of ZMYND10, as opposed to off-target effects. For detailed analysis, we focused on a -7bp deletion mutant line (*Zmynd10* c.695_701 p.Met178Ilefs*183), which results in a frame shift with premature termination. Generation of a null allele was verified by ZMYND10 immunoblotting of testes extracts (postnatal day 26, P26) and immunofluorescence of multiciliated ependymal cells and lung cryosections (**Figure 1B-D)**

Zmynd10 mutant mice displayed several clinical features of PCD including heterotaxia, progressive hydrocephaly and chronic mucopurulent plugs in the upper airways, all features consistent with defects in ciliary motility (**Figure 1E-H, Figure 1-figure supplement 2**). This was directly confirmed by high-speed video microscopy of ependymal cells, where cilia of normal number and length were present but failed to move (**Movie 1,2,3,4, Figure 1-figure supplement 3**). Ultrastructure analysis of tracheal cilia axonemes revealed an absence of both outer and inner dynein arms (**Figure 1F**). The hydrocephaly phenotype was particularly pronounced on a C57BL6/J background and the majority of mutants died around weaning (P17-P21). On outbred backgrounds, male infertility and sperm immotility were also noted in homozygous mutant animals (**Figure 1-figure supplement 2, Movie 5,6**). These findings demonstrate that ZMYND10 functions are exclusively required in most motile ciliated cell lineages.

Mis-assembled dynein motors are blocked from entering cilia and cleared in *Zmynd10* mutants

We analysed expression of dynein subunits in different postnatal tissues by immunofluorescence and immunoblotting from *Zmynd10* mutants, focusing on ODA components for which the most robustly validated immunoreagents exist, to assess whether ZMYND10 loss impacts ODA levels. In adult trachea (P26) and oviducts (P26-30), total levels of the ODA HCs DNAH9 and DNAH5, as well as ICs DNAI1 and DNAI2 were reduced by immunoblot (**Figure 2A,B**) and immunofluorescence (**Figure 2C,D**). In agreement with recent studies(Cho et al., 2018), no alteration in dynein transcripts were detected by RT-qPCRs on mutant oviduct (P12) total RNA, supporting the findings that the zinc-finger MYND domain of ZMYND10 plays cytoplasmic molecular scaffold functions other than a nuclear transcriptional role (**Figure 2E)**. Critically, immunoblots of P7 *Zmynd10* mutant oviduct lysates, an early stage corresponding to synchronized multicilial axonemal elongation (Dirksen,

1974), showed a laddering of DNAH5 products using an antibody raised against an N-terminal epitope, indicating post-translational destabilization of DNAH5 in the absence of ZMYND10 (**Figure 2F**).

These observations raise the possibility that in the absence of ZMYND10, individual dynein subunits are initially synthesised during cytoplasmic pre-assembly before a quality-control response is triggered to clear stalled dynein motor assembly intermediates that fail to reach the mutant axonemes. The process of mammalian cytoplasmic pre-assembly in terms of dynamics of localization and levels of dynein subunits has been previously documented(Diggle et al., 2014). 'Immature' cells stain strongly for dynein subunits within the cytoplasm, they appear rounder and their cilia are apparently shorter than those cells in which dynein subunits exclusively stain the ciliary compartment. Using Sentan as an independent marker for 'mature' motile cilia, we were able to detect a strong, focused signal at the tips of cilia with exclusively ciliary staining of axonemal dyneins (**Figure 3A,** lower left inset). Sentan is a component of the apical ciliary crown structure of mature motile cilia, where peripheral singlet microtubules are capped by electron dense material abutting the membrane (Kubo et al., 2008). In contrast, in cells without clear apical Sentan signal, shorter cilia and cytoplasmic staining (DNAI2, DNALI1) were observed, consistent with these cells being 'immature' and in the process of assembling dynein motors and cilia (**Figure 3A,** upper right inset). We therefore postulate that these dynamic patterns of dynein subunits represent 'mature' and 'immature' cells during assembly of motile cilia, which we can see in cells isolated from nasal turbinates of control mice (3B middle and upper panels, respectively). In *Zmynd10* mutants*,* no apparent defects in ciliary length or number were observed (**Figure 1-figure supplement 3**) however outer or inner arm dyneins fail to incorporate into mature ciliary axonemes. Importantly, no cytoplasmic accumulations were noted in 'mature' ciliated cells (**Figure 3B** panels with arrows). Surprisingly, cytoplasmic staining was observed in both 'immature' control and *Zmynd10* mutant cells (**Figure 3B,** arrowheads). A similar staining pattern was observed for DNALI1 (**Figure 3C**) indicating ODA and IDA dynein subunit precursors are initially synthesised normally, further supporting that ZMYND10 loss does not impact their transcription or translation. Instead, loss of ZMYND10 leads to dyneins being robustly cleared when their pre-assembly is perturbed.

ODA and IDA complexes are defective and unstable in the absence of ZMYND10.

As cytoplasmic staining for DNAI2 and DNAH5 was detected in *Zmynd10*$^{-/-}$ immature respiratory cells, suggesting that they were initially synthesized, we sought to verify if they were assembled into complexes using the *in situ* proximity ligation assay (PLA). In control immature human nasal brush epithelial cells, we detected PLA signals consistent with DNAI2 and DNAH5 existing in both cytoplasmic and axonemal complexes (**Figure 4A**). However, we detected a highly reduced number

of PLA positive foci in nasal epithelial cells of P7 *Zmynd10*$^{-/-}$ mice, with complexes restricted entirely to the cytoplasm in contrast to the strong axonemal staining observed in similarly staged controls **(Figure 4B, Figure 4-figure supplement 1**). To directly examine the interactions between ODA IC and HC subunits, we immunoprecipitated endogenous DNAI2 (IC2) from postnatal testes (P26), trachea (P7 and P90) and oviduct (P7) extracts from *Zmynd10*$^{-/-}$ animals. DNAI2 co-precipitated DNAI1 (IC1) at similar levels from both wild type and mutant P26 testes extracts (**Figure 4C**). This indicated that loss of ZMYND10 does not primarily impact IC subunit heterodimerization or stability during the assembly process. Similarly, the relative enrichment of DNAI2 changed very little between mutant and wild type P7 oviduct and trachea mutant extracts. In contrast, we observed significantly reduced co-immunoprecipitation of DNAH5 by DNAI2 in P7 oviduct and trachea mutant extracts (0.47 and 0.56 fold reduction respectively, normalized to total levels, **Figure 4D,E** and **Figure 4-figure supplement 1B,C**). Moreover, we observed similar degradative bands (arrowheads) for DNAH5 in the mutant samples indicating that any DNAH5 that is incorporated may be poorly folded and unstable, in the absence of ZMYND10. We hypothesize that this reduced association between the two subunits is due to the HC subunit being in an assembly incompetent, unstable state such that any substandard complex would be targeted for subsequent degradation (**Figure 4F**).

ZMYND10 loss also leads to absent IDA motors from human, fly and mouse cilia(Cho et al., 2018; Kobayashi et al., 2017; Kurkowiak et al., 2016; Moore et al., 2013; Zariwala et al., 2013). To bypass the limitation of robust immunoreagents for IDA detection, we used label-free quantitative proteomics comparing postnatal testes extracts from P25 control and *Zmynd10* mutant littermates. ZMYND10 is highly expressed in the cytoplasm of round and elongating spermatids, as well as maturing sperm (**Figure 5A**). In the absence of ZMYND10, mature sperm form but lack expression of outer and inner dynein subunits (**Figure 5B).** At P25, we hypothesized that synchronized spermiogenesis and flagellar extension at this stage would correspond with cytoplasmic pre-assembly of flagellar precursors. Whilst protein expression profiles were not different between mutant and controls for differentiation, meiosis and cell death markers (**Supplementary File 1**), the expression profile for the motility machinery showed specific and significant changes wherein almost all the axonemal dynein HCs (outer and inner) detected were reduced whilst the other axonemal dynein subunits were generally not significantly changed (ICs WDR78 and DNAI1, DNAI2) (**Figures 5D, Figure 5-figure supplement 1)**. This is distinct from previous observations in *Chlamydomonas,* where loss of DNAAFs (DNAAF1, 2 and 3) impacting HC stability generally led to an aberrant cytosolic accumulation of IC subunits(Mitchison et al., 2012), highlighting a key difference between the two model systems. Components of the radial spokes (RS) and dynein regulatory complex (DRC) were also unchanged (**Figure 5D**). Interestingly, several DNAAFs including the co-chaperones DNAAF4 and

DNAAF6 were moderately but significantly up regulated in *Zmynd10* mutants suggestive of a proteostatic response to counter aberrant pre-assembly as it progresses.

A ZMYND10-FKBP8-HSP90 complex mediates maturation of dynein heavy chains

To further understand how ZMYND10 regulates stability of axonemal dynein HC subunits, we aimed to generate an endogenous ZMYND10 interactome in P30 mouse testes using two validated commercial ZMYND10 polyclonal antibodies followed by mass-spectrometry (AP-MS, **Supplementary File 2**). Overlapping interactors in the endogenous affinity purifications of ZMYND10 included ODA HCβ DNAH17 (fold enrichment: 5.8x (P), 2.9x (S); p>0.05), HSP90 (1.5x, 1.8x; p>0.01) and the well-characterized immunophilin FKBP8 (FK506-binding protein (FKBP) family member) (6.2x, 8.2x; p>0.001), which can act as an HSP90 co-chaperone (**Figure 6A**).

This suggested a novel association between a mammalian DNAAF, putative 'client' dynein heavy chain and the ubiquitous HSP90-FKBP8 chaperone complex during cytoplasmic pre-assembly *in vivo.* To validate these interactions, we immunoprecipitated endogenous ZMYND10 and FKBP8 from control versus mutant testes samples (P30: **Figure 6B**) and cultures of differentiating human tracheal epithelial cells (D17 ALI1: **Figure 6C**), both during cytoplasmic pre-assembly. Indeed, we confirmed that ZMYND10 interacted with FKBP8 and HSP90, but not with other DNAAFs, including previously identified interactor LRRC6 (**Figure 6B**). We also corroborated associations between FKBP8, ODA HCα DNAH5, HSP90 and ZMYND10 using human Air-Liquid Interface (ALI) cultures and P7 oviducts (**Figure 6C,D**), as we failed to find specific immunoreagents against testes ODA HC isoforms (i.e. ODA HCβ DNAH17 or HCα DNAH8). Taking step-wise ODA macromolecular assembly into account, we found that whilst DNAI1 co-immunoprecipitated DNAH5, it did not immunoprecipitate either ZMYND10 or FKBP8 (human ALI tracheal cells D17: **Figure 6C**). Together our data suggests that the DNAI1-DNAH5 interaction occurs in a complex that is distinct and downstream from the FKBP8-DNAH5-ZMYND10 complex, as supported by our DM-CHX experiments in which both subunits are destabilized after 24 hours drug treatment.

We verified the interactions between ZMYND10 and FKBP8 as well as HSP90 using tagged ZMYND10 affinity purifications from primary ciliated HEK293T cells (**Figure 7B**). In agreement, direct interaction between the N-terminus of FKBP8 and MYND domains of ZMYND6/PHD2 (Barth et al., 2009) and ZMYND20/ANKMY2 (Nakagawa et al., 2007) have also been reported. To characterize the complex between FKBP8 and ZMYND10 further, we mapped their interaction interface and assessed its potential biological relevance by generating point mutations in ZMYND10 (**Figure 7A**). The W423A mutation falls within the MYND domain and is predicted to functionally disrupt one of two Zn^{2+}-fingers in the MYND domain. Located just before the MYND domain, the T379C PCD patient

mutation (Zariwala et al., 2013) failed to disrupt binding to LRRC6, suggesting some other underlying pathogenic mechanism exists for this mutation, one which we hypothesize could involve FKBP8. Affinity purification of ZMYND10-turboGFP variants from HEK293T cells revealed that both point mutations abolish endogenous FKBP8 binding (**Figure 7B**). These results indicate that the interaction interface for FKBP8 extends beyond the MYND domain of ZMYND10, consistent with recent deletion mutations described in *medaka* capable of functional rescue (Kobayashi et al., 2017) and suggest that loss of ZMYND10-FKBP8 interaction may underlie the pathogenic effect of the T379C PCD mutation.

FKBP8 is a peptidyl-prolyl isomerase (PPIase), which catalyzes cis-trans isomerization of proline peptide groups and is one of the rate-determining steps in protein folding. To test whether its PPIase activity is critical for stabilization of dynein HCs, we treated immature day 17 and mature day 60 (D17 and D60 ALI) human tracheal epithelial cell cultures with a specific PPIase inhibitor DM-CHX (Edlich et al., 2006) for 24 hours and assayed extracts for stability of ODA subunits by immunoblotting. Immature cultures were very sensitive to FKBP8 inhibition, where cytoplasmic levels of DNAH5 were reduced to ~10% of control levels after DM-CHX (150µM). In mature cells, fully assembled complexes within cilial axonemes were less sensitive to DM-CHX treatment (**Figure 7C and 7D**). Surprisingly, a very striking destabilization of DNAI1 was also observed in immature cultures under these conditions. This supports the possibility that a transient requirement of the PPIase activity of FKBP8 is necessary for the folding and/or stability of axonemal dyneins in the cytoplasm.

Immunofluorescence of mouse tracheal epithelial cells (mTECs) shows that treating parallel cultures once they have differentiated (D3 ALI, 14 days vehicle followed by 7 days DM-CHX), or as they begin to differentiate (D3 ALI, 14 days DM-CHX followed by 7 days vehicle) have drastically different outcomes (**Figure 7E**). In agreement with immunoblot data, inhibiting the PPIase activity of FKBP8 in mature ALI cultures does not affect motility or levels of DNAH5 or DNAI2, whilst early inhibition drastically reduces the levels of these ODA components and abolishes motility (**Figure 7E**).

A successive set of complexes are involved in multiple steps of axonemal dynein assembly.

In the chaperone cycle of HSP90, PPIs like FKBP8 are part of the intermediate stage where HSP90 is bound to the client protein and ATP. Co-chaperones containing a p23-like domain enter at the last stage of the chaperone cycle when ATP is hydrolysed and client and co-chaperones are released from HSP90(J. Li and Buchner, 2013). As LRRC6 contains a p23/CS-like domain and was previously reported to interact with ZMYND10(Moore et al., 2013; Zariwala et al., 2013), we went on to investigate the effect of LRRC6 on ZMYND10 binding to FKBP8.

Expression of myc-LRRC6 and ZMYND10-turboGFP followed by affinity purification with a monoclonal antibody to turboGFP shows that all ZMYND10 variants tested interact with LRRC6, extending on previous studies (Zariwala et al., 2013). Interestingly, the presence of myc-LRRC6 significantly decreased the association of ZMYND10 to FKBP8 (**Figure 8A**). These results are consistent with the canonical roles of p23 co-chaperones and suggest that its presence advances the HSP90 chaperone cycle releasing all co-chaperones and thus promoting FKBP8 dissociation from ZMYND10. Whilst we have been unable to confirm endogenous interaction of ZMYND10 and LRRC6 (**Figure 6A, 6B, Supplementary File 2**), we note that LRRC6 levels are decreased (-7.2 fold change, p= 0.023, **Figure 5D, Supplementary File 1**) in *Zmynd10* mutant testes suggesting some functional interaction exists during cytoplasmic pre-assembly, highlighting the transient nature of some of these interactions *in vivo*.

Taken together our results suggest that ZMYND10, firstly with FKBP8 and subsequently with LRRC6, likely participates in an HSP90 chaperone cycle of common clients, the axonemal dynein heavy chains. LRRC6 may promote the final maturation and release of clients and co-chaperones onto subsequent chaperone complexes, including the R2TP and R2TP-like complexes associated with additional subunits such as the IC1/2 heterodimers, for the next stages of assembly (**Figure 8B**). Future studies will determine how HSP90 may be targeted to specific stages of dynein pre-assembly, but competitive binding through the conserved C-terminal motif MEEVD of HSP90 between discrete HSP90-co-chaperone-client complexes may confer directionality (Back et al., 2013; Blundell et al., 2017; Lage et al., 2018; Martino et al., 2018; Yamaguchi et al., 2018). Stalling of the folding process will likely trigger degradation of all folding intermediates regardless of the initial client protein recruited by the chaperone machinery.

Discussion:

Motile cilia are highly complex structures comprising of hundreds of mega-Dalton scale molecular assemblies. Axonemal dynein motors represent the largest and most complex of such motile ciliary components. Their coordinated transcription, translation, assembly and transport is critically linked to ciliary function. The cell appears to have evolved a dedicated chaperone relay system involving multiple assembly and transport factors to execute distinct steps for their pre-assembly, sometimes in a tissue- or ciliary domain-specific manner (Dougherty et al., 2016; Fliegauf et al., 2005; Yamaguchi et al., 2018).

In the present study we reveal that the DNAAF ZMYND10 co-operates with the ubiquitous co-chaperone FKBP8 and chaperone HSP90 to mediate a key step in the pre-assembly pathway, specifically maturation of axonemal dynein heavy chains. Using multiple motile ciliated tissues, including trachea, oviduct and testes, from *Zmynd10* null mouse models, we observed reduced protein abundances for ODA HCs (DNAH5, DNAH9) and ICs (DNAI1 and DNAI2). Proximity ligation assays and immunopurification of endogenous components suggest that unstable intermediates of axonemal dynein ODA HCs are primarily affected and unable to fully associate with the IC heterodimers which are subsequently degraded in *Zmynd10* mutants. We provide evidence that the PPIase activity of FKBP8 is required to stabilize wild type axonemal dynein assemblies. Specific pharmacological inhibition of FKBP8 PPIase activity phenocopies the motility defects observed in *Zmynd10* mutants. We also confirm that LRRC6 may participate transiently at possibly later stages in the ZMYND10 dependent HSP90 chaperone cycle. Finally, mutations of *ZMYND10* that impair its ability to interact with the FKBP8-HSP90 chaperone system but not with LRRC6, provide a molecular explanation for a previously unresolved PCD disease-causing variant (Zariwala et al., 2013).

HSP90 is emerging as a central feature in the post-translational maturation of axonemal dynein motors, through at least two distinct regulatory modules. The first one involves the multi-functional R2TP complex (RUVBL1, RUVBL2, RPAP3, PIH1D1), which is a well-characterized co-chaperone of HSP90 in the assembly of several multimeric protein complexes (Kakihara and Houry, 2012; Morgen et al., 2015). Recent reports have highlighted the importance of PIH-domain containing DNAAFs (DNAAF2 and DNAAF6), RPAP-domain containing SPAG1 as well as Reptin (RUVBL2) and Pontin (RUVBL1) as regulators of cilia motility (Desai et al., 2018; Dong et al., 2014; Lage et al., 2018; Y. Li et al., 2017; Olcese et al., 2017; Omran et al., 2008; Paff et al., 2017; Tarkar et al., 2013; Yamaguchi et al., 2018). All of these factors bear homology to components or form part of the multi-functional R2TP complex. Functional genetic analysis of the four PIH zebrafish paralogues revealed distinct and

overlapping DNAAF functions in pre-assembly of specific subsets of axonemal dynein motors, in a tissue-specific as well as axonemal domain-specific manner (Yamaguchi et al., 2018). Biochemical evidence from endogenous affinity purification of an R2TP adaptor, WDR92 further revealed physical associations of heavy and intermediate chains of ODA and IDA subunits with R2TP (Lage et al., 2018). Collectively, these studies link dynein assembly factors to a cilial-specific configuration of the HSP90-R2TP complex. However, further biochemical studies are needed to define how these different cilial-configurations of R2TP-HSP90 and dynein clients interact during the chaperone cycles operative during axonemal dynein pre-assembly. Our study uncovers a second cilial-specific configuration of the HSP90 chaperone machinery involving FKBP8 via ZMYND10 in the processing of client axonemal dynein heavy chains in all motile ciliated tissues studied (**Figure 8B**). We show that the unchanged transcript levels do not correlate with the reduced protein levels of axonemal dynein HCs (**Figure 2D**) and that unstable heavy chain folding intermediates in *Zmynd10* mutant extracts likely result from degradation of fully translated, improperly folded axonemal dynein HCs. Our results suggest that ZMYND10 directs and drives an FKBP8-HSP90 cycle, likely involving LRRC6, aiding the maturation of axonemal dynein HC clients required for their post-translational stability.

Our multipronged approach using immunofluorescence, proteomic and endogenous interaction studies all indicate that axonemal dynein HCs are the primary clients of ZMYND10. This is in contrast to recent studies suggesting that ZMYND10's primary targets are the ODA ICs, DNAI1 and DNAI2 (Cho et al., 2018; Kurkowiak et al., 2016). Initially, neither the levels of DNAI1 and DNAI2 (**Figure 5D, Supplementary File 2**), nor heterodimer formation (**Figure 4C**) are significantly affected during cytoplasmic pre-assembly in *Zmynd10* mutants. Moreover, our unbiased label-free quantitative proteomics shows that ZMYND10 loss also specifically impacts IDA HC stability whilst other subunits or structures remain mostly unaffected. This is distinct from the response seen in PCD models specifically affecting ODAs wherein complete lack of or misfolding of a single heavy chain in the case of DNAH5 results in a very specific and limited loss of outer dynein arms only: in *DNAH5* patients, DNALI1 is still found in the ciliary axonemes and IDAs visible by TEM(Loges et al., 2008). The primary defects we observe support the hypothesis that aberrant HC-IC subunit association and/or the misfolded HC polypeptides themselves trigger a robust proteostatic response leading to clearance of non-functional ODA and IDA complexes to mitigate cellular protein stress.

Our study goes towards addressing a long-standing question of where dynein pre-assembly occurs within the cytoplasm. Our interaction and mutational studies define a novel ZMYND10-FKBP8-HSP90 complex functioning in dynein pre-assembly, where FKBP8 could tether HC folding to endomembranes. The participation of FKBP8-HSP90 chaperone complex in protein folding, activation and clearance has been extensively documented (Banasavadi-Siddegowda et al., 2011;

Barth et al., 2009; 2007; Edlich et al., 2005; Hutt et al., 2012; Saita et al., 2014; Taipale et al., 2014; Wang et al., 2006). Given the role of this complex in folding and maturation of CFTR on the cytosolic face of the ER (Hutt et al., 2012; Wang et al., 2006), it raises the possibility that during early stages of pre-assembly, axonemal dynein heavy chains could also be localized to the cytosolic face of the ER through ZMYND10's association with FKBP8. Future work should be directed to further pinpoint where different assembly steps occur within the cytoplasm. It would be tempting to speculate that properly folded dynein HCs are subsequently exchanged in the recently described dynamic cytoplasmic puncta containing rapidly fluxing DNAAFs and less mobile dynein subunits as shown for DNAI2 and DNALI1, structures termed dynein assembly particles or DynAPs(Huizar et al., 2017; Y. Li et al., 2017). This 'phase separated organelle' model is attractive as increasing local concentration of specific DNAAF complexes could help overcome the apparently low binding affinities between different DNAAFs except in these molecular condensates. Indeed, we have been unable to capture endogenous interactions between LRRC6 and ZMYND10 *in vivo* (**Figure 6A, 6B** (Moore et al., 2013; Zariwala et al., 2013)), suggesting their physiological interactions may be highly transient or temporally restricted, as opposed to existing in stable complexes.

Taken together, we propose a revised model of the dynein preassembly pathway (**Figure 8B**), where multiple roles for HSP90 are emerging. Here, ZMYND10 acts a novel co-chaperone of the ubiquitous FKBP8-HSP90 chaperone complex for axonemal dynein HC subunit maturation. Mature, assembly-competent HCs are then handed-off to a subsequent chaperone complex, likely the R2TP complex to allow for stable associations with other subunits such as the IC1/2 complex, in a ZMYND10-independent step. Working together, this chaperone relay ensures efficient assembly of functional dynein complexes for subsequent ciliary targeting. Given the critical role ZMYND10 plays in dynein assembly, we propose a novel alias, DNAAF7 for ZMYND10. Our work on ZMYND10 shows that the biosynthesis and quality control of dynein motors relies on an elaborate proteostasis network. Perturbations to this network by pharmacological means or due to genetic defects can disrupt motor assembly leading to PCD. This represents a paradigm shift in our understanding of PCD pathogenesis. We propose that the motile ciliopathy Primary Ciliary Dyskinesia (PCD), when caused by defects in dynein preassembly should be considered a cell-type specific protein misfolding disease, which may be amenable to therapy by modulation of the cellular proteostasis network.

Acknowledgements:

The authors thank IGMM technical services, the IGMM Advanced Imaging and CBS animal facilities for advice and technical assistance. We are very grateful to Masayuki Amagai, Hiroshi Hamada, Akiharu Kubo, Yasuko Inaba, Friedhelm Hildebrandt, and Heon Yung Gee for generously sharing reagents and to Chrisostomos Prodromou for helpful discussions. This work was supported by core funding from the MRC (MC_UU_12018/26) (to GRM, PLY, DOD, PAT, MAK, PM), and a Science Foundation Ireland grant (SIRG) (to AGM and AvK). The mass spectrometry proteomics data have been deposited to the ProteomeXchange Consortium via the PRIDE partner repository with the dataset identifier PXD006849.

The authors declare no competing financial interests.

Abbreviations

ALI	air-liquid interface
AP-MS	affinity purification mass spectrometry
CRISPR	Clustered Regularly Interspaced Short Palindromic Repeats
D	day post-airlift (ALI)
DNAAF	dynein axonemal assembly factor
DRC	dynein regulatory complex
FKBP	FK506-binding protein
HC	heavy chain
HSP	Heat Shock Protein
IAD	inner arm dynein
IC	intermediate chain
IDA	inner dynein arm
LC	light chain
mTEC	mouse tracheal epithelial cells
MYND	myeloid, Nervy, and DEAF-1 domain
OAD	outer arm dynein
ODA	outer dynein arm
P	postnatal day
PCD	primary ciliary dyskinesia
PPIase	peptidyl-prolyl isomerase
PLA	proximity ligation assay
R2TP	RUVBL1, RUVBL2, TAH1, PIH1 complex
RSP	radial spoke proteins
TEM	transmission electron microscopy

Figure legends:

Figure 1. Loss of *Zmynd10* in mice results in a PCD phenotype.

(A) Schematic illustrating the null allele generated by a -7bp CRISPR deletion in *Zmynd10* exon 6. (B) Immunoblots from testes extracts from postnatal day 26 (P26) control and mutant male mice show loss of ZMYND10.
(C, D) Immunostaining for ZMYND10 reveals a complete loss of signal in multiciliated ependymal cells (C) and lung cryo-sections (D). Multicilia are marked with acetylated α- tubulin (C).
(E) Neonatal *Zmynd10* mutants display hydrocephaly; the white arrowhead points to doming of the head. See also Figure 1- figure supplement 2E.
(F) TEM of tracheal ciliary axoneme cross-sections shows a lack of axonemal ODA (white arrowhead) and IDA (black arrowhead) dynein arms in mutants.
(G) Representative image of a gross dissection of lungs show *situs inversus totalis* in mutants. See also Figure 1- figure supplement F.
(H) H&E staining of coronal sections of nasal turbinates reveals mucopurulent plugs in mutants. Scale bars in (C)=5μm, in (D)=100μm, in (F)=100nm.

Figure 1- figure supplement 1. Generation of *Zmynd10* mutant mice by CRISPR genome editing.

(A) Schematic of *Zmynd10* mouse locus (ENSEMBL: ENSMUSG00000010044) and guide design targeting critical exon 6 which were cloned into px330 (Addgene:#42230)(Cong et al., 2013).
(B) Validation of activities of gRNAs to generate double-stranded breaks were initially tested in HEK293 cells by using a reporter to assay reconstitution of EGFP upon cleavage (Addgene: #50716)(Mashiko et al., 2014).
(C) Table summarizing pronuclear microinjection rounds for generating *Zmynd10* mutants.

Figure 1- figure supplement 2. Detailed phenotypic analysis of *Zmynd10* mutants.

(A) Representative image of a testis from *Zmynd10* mutant and wild type control (P150).
(B) As a result of defects in flagellar development, mutants have smaller testes (mean +/- s.e.m, n=3 males/genotype). *Zmynd10* mutants have lower sperm density (mean +/- s.e.m, n=3 males/genotype).
(C) *Zmynd10* mutant sperm have reduced motility. Arrows point to static/paralyzed sperm in mutants. Scale bars= 50μm.
(D) By immunofluorescence, staining of DNAI2 and DNALI1 is absent along *Zmynd10*$^{-/-}$ flagella Arrowhead in wild type point to the annulus region and flagellar tip. In the mutant, the arrowhead points to the annulus.
(E) Coronal vibratome sections of brains show *Zmynd10* mutants display dilated lateral ventricles (arrowhead) due to hydrocephaly.
(F) *Zmynd10* mutants display heterotaxy defects. Arrowheads denote direction of the heart's position, which is reversed in the mutants; numbers denote lobes of the lungs (1,2 and 3 correspond to upper, mid and lower lobes of the right lung; 4 and 5 correspond to the upper and lower lobes of the left lung).

Figure 1- figure supplement 3. No gross ciliary defects are seen in *Zmynd10* mutants.

(A) Transmission electron micrographs (TEM) of tracheal multiciliated cells from wild type and mutant female mice (P9). Arrows point to cilia on luminal surface of the cells; basal bodies appear correctly docked in the mutant cells similar to controls. Scale bar = 2μm.
(B) Immunostaining for cilia (acetylated α-tubulin) and apical F-actin (phalloidin) reveals no cytoskeletal gross defects in *Zmynd10* mutants. Scale bars = 10μm

Figure 2. Global post-transcriptional destabilization of dyneins occurs in *Zmynd10* mutant motile ciliated tissues.

Immunoblots of whole protein extracts from trachea P26 (A) and P30 oviducts (B) show reduced abundance of ODA subunits HC-γ, HC-β (DNAH5 and DNAH9), IC1 and IC2 (DNAI1 and DNAI2). Immunofluorescence of trachea (C) and oviduct (D) tissue sections show loss of axonemal DNAH5 and DNAI2 staining as well as reduced total abundance in *Zmynd10* mutants compared to controls. Brightfield is included in oviduct merge panel (D) to highlight absence of staining in cilia in *Zmynd10* mutants. Scale bars in (C) & (D) = 50µm

(E) No significant changes are detected in levels of dynein transcripts by quantitative RT-PCR of (*Dnah5, Dnali1*) normalized to (*Tbp)* in P12 *Zmynd10* mutant oviducts (n=3/genotype, dark grey *Zmynd10* mutants).

(F) During early motile ciliogenesis, mildly reduced levels and laddering consistent with degradative, misfolded intermediates (arrowheads) of ODA HC-γ DNAH5 are detected in *Zmynd10* mutant oviducts (P7). These will be subsequently cleared as tissue differentiation proceeds.

Figure 3. Loss of ZMYND10 perturbs sub-cellular distribution and levels of dynein complexes during pre-assembly.

(A) Z-projection through healthy human donor nasal brush immunofluorescence shows a mix of 'mature' motile ciliated cells (lower inset, arrow) with exclusively axonemal staining of dynein subunits (DNAI2 green, DNALI1 magenta) and strong foci of SENTAN (red) at cilial tips, as well as 'immature' cells having cytoplasmic staining of dynein subunits and no SENTAN (right inset, arrowheads). Scale bar =10µm.

(B) Nasal brush immunofluorescence from *Zmynd10* mice shows components of outer arm dyneins (DNAH5, DNAI2) are initially expressed in apical cytoplasm of immature mutant cells (arrowheads) but subsequently undergo 'clearance' in mature cells (lower panels, arrows), whilst all complexes exclusively translocate into cilia in control mature cells (middle panels, arrows).

(C) Inner arm dynein component DNALI1 is expressed and apically arrested in immature mutant cells (arrowhead) and unlike controls, will get subsequently get cleared along with the ODA IC, DNAI2, in mature mutant cells. Scale bars =5µm.

Figure 4. Sequential cytosolic assembly of outer arm dynein components occurs in mammalian motile ciliogenesis in a process requiring ZMYND10.

(A,B) Z-projections of Proximity Ligation Assay (PLA) on human donor (A) or mouse P7 (B) nasal brush biopsies confirming ODA subunits (mouse IC2/DNAI2 and HC-γ/DNAH5) are pre-assembled in the cytoplasm of mammalian multiciliated cells. Control (antibody only control, Ab control) sections incubated with only DNAH5 show no PLA signal. Red spots denote individual ODA complexes (<40 nm) that appear as peri-nuclear foci in immature cells (arrowhead) and translocate to cilia in mature cells (arrow). (B) In *Zmynd10* mutant cells, reduced number of foci are observed and restricted only to the cytoplasm, highlighting defects in cytoplasmic pre-assembly. GRP94 was used as a pan-cytosolic marker (A) or phalloidin for apical actin ring (B). Nuclei are stained with DAPI (blue). See also Figure 4- figure supplement 1A for mouse IC2/DNAI2 and HC-β/DNAH9 PLA. Scale bars in (A)=5µm and (B)=10µm

(C) Endogenous Immunoprecipitation of DNAI2 from P26 Testes extracts reveals no defects in DNAI2 association with its heterodimeric partner DNAI1 in *Zmynd10* mutants.

(D) Endogenous Immunoprecipitation of DNAI2 from P7 oviduct extracts show disruption in subsequent association between DNAI2 and DNAH5 in mutants compared to controls as quantified by intensities of the DNAH5 pull-down bands (E). Arrowheads show predicted degradative or misfolded intermediates of DNAH5 polypeptide in the mutants only. Numbers to the right of panels denote protein molecular weight in kDa. See also Figure 4- figure supplement 1B,C for analysis in P7 and P90 trachea.

(E) Ratio of mutant versus wild type fold enrichment (from 4D, Figure 4- figure supplement 1B:

IP/input) for DNAI2 and DNAH5, normalized for differences in stability in input, as well as amount of DNAH5/DNAI2 complexes.
(F) Schematic of axonemal ODA showing the intermediate chain heterodimers (IC) bind normally to heavy chains (HC) to form the entire motor complex in controls (green) and that this association is perturbed in mutants (red).

Figure 4- figure supplement 1. Sequential cytosolic assembly of outer arm dynein components occurs during mammalian motile ciliogenesis in a process requiring ZMYND10.

(A) Z-projections of Proximity Ligation Assay (PLA) on mouse P7 nasal brush biopsies confirming that ODA subunits (mouse IC2/DNAI2 and HC-β/DNAH9) are pre-assembled in the cytoplasm. Control (antibody only control, Ab control) sections were incubated with only DNAH9 antibody and show no PLA signal. Red spots denote individual ODA complexes (<40 nm) in control cells and cilia. In *Zmynd10* mutant cells, reduced number of foci are observed and restricted only to the cytoplasm, highlighting defects in cytoplasmic assembly. Phalloidin was used to mark the apical actin ring. Nuclei are stained with DAPI (blue). Scale bar =10µm.
(B, C) Immunoprecipitation of DNAI2 from P7 trachea extracts show disruption in subsequent association between DNAI2 and DNAH5 in mutants compared to controls, as quantified by intensities of the DNAH5 pull-down bands (Figure 4E). In contrast, in P90 adult *Zmynd10* mutant trachea (C), levels of DNAI2 are profoundly affected (input), and negligible complexes can be purified.

Figure 5. Early and specific defects in axonemal dynein heavy chain stability are observed in *Zmynd10* mutants during cytoplasmic assembly.

(A) Immunofluorescence of ZMYND10 in control and mutant adult testes (P150) in asynchronous seminiferous tubules (arrowhead). (A) ZMYND10 is strongly expressed in primary spermatocytes and spermatids, where it is restricted to the cytoplasm and never in developing sperm tails. This staining is lost in mutants. Nuclei are stained with DAPI. Scale bar = 100µm.
(B) Cross-sections of similarly staged seminiferous tubules reveal similar developmental staging of sperm between adult control and mutants, but loss of DNAI2 (ODA) and DNALI1 (IDA) proteins from cytoplasm and axonemes (arrowhead) of mutant sperm. Nuclei are stained with DAPI. Scale bars = 50µm, 100µm.
(C) Schematic summarizing mouse spermatogenesis which is initially synchronized postnatally (stages shown to right), before occurring in asynchronous waves across seminiferous tubules. Axonemal dynein pre-assembly in the cytoplasm occurs in the spermatid stage around P25 and continues till flagellogenesis at P30.
(D) Unbiased quantitative proteomics of control and mutant testes (elongated spermatid: P25) reveal that loss of ZMYND10 leads to a primary reduction in abundance of all dynein HC subunits during cytoplasmic pre-assembly, whilst other components remain initially unaffected at this stage. Yellow diamonds highlight significantly ($p<0.05$) changed hits based on LFQ intensity between *Zmynd10* mutants and wild type littermates (n=3/genotype). Schematic below highlights fold change of specific subunits on given dynein arms. Some heavy chains had specific multiple isoforms detected (DNAH7b/c and DNAH12 (E9QPU2*, F6QA95, Q3V0Q1†). See also Supplementary File 1. Key: IAD: inner arm dynein; OAD: outer arm dynein; DNAAFs: dynein axonemal assembly factors; RSP: radial spoke protein; DRC: dynein regulatory complex.

Figure 5- figure supplement 1. Peptide intensities across the axonemal dynein heavy chains reveal profound and significant decreases, whilst other dynein subunits are not affected.

Intensities of peptides detected by mass spectrometry from P25 testes whole proteome analysis (Figure 5D) are plotted across the polypeptide lengths for individual axonemal dynein subunits (ODA

and IDA-HCs, ODA-ICs, ODA-LC). TTC25 (ODA-docking complex) and cytoplasmic dynein 1 and 2 heavy chain polypeptides are used as controls. Axonemal dynein heavy chains specifically show reduced peptide intensities in *Zmynd10* mutant testes samples (red) compared to controls (blue). All the other proteins tested have comparable peptide intensities between mutant and control samples.

Figure 6. ZMYND10 interacts with a novel chaperone relay at a distinct stage of dynein heavy chain stability during cytoplasmic assembly.

(A) Summary schematic of affinity purification-mass spectrometry (AP-MS) analysis of endogenous ZMYND10 interactomes from P30 mouse testes, overlapping between two commercial polyclonal Sigma (S) and Proteintech (P) antibodies. See also Supplementary File 2.
(B) Endogenous ZMYND10 affinity purification with two validated ZMYND10 antibodies from *Zmynd10* control and mutant P30 testes extracts confirm the ZMYND10 interaction with FKBP8 and HSP90AB1 (S only) in control samples. These interactions are not found in mutant samples lacking ZMYND10, serving as specificity controls. An *in vivo* interaction between ZMYND10 and LRRC6, as well as with DNAAF1, was not detected in reciprocal endogenous immunoprecipitations in P30 control testes extracts, using rIgG as a control.
(C) Endogenous FKBP8 and DNAI1 immunoprecipitations in differentiating healthy human donor tracheal epithelial cultures (D17 ALI) both show binding of client DNAH5, the rest of the complexes are distinct, suggesting they act at sequential steps of assembly.
(D) Endogenous ZMYND10 immunoprecipitation of client DNAH5 and chaperone HSP90, but not HSP70 from differentiating oviduct epithelial tissue (P7) using rIgG as a control. Protein molecular weights displayed in KDa.

Figure 7. Ubiquitous FKBP8 actively participates in axonemal dynein heavy chain stability via its interaction with ZMYND10.

(A) Summary of mutations generated in ZMYND10-tGFP by site-directed mutagenesis to disrupt the binding interface for FKBP8, including the W423A mutation predicted to functionally disrupt one of two Zn^{2+}-fingers in the MYND domain and the T379C PCD patient mutation (Zariwala et al., 2013), lying just before the MYND domain.
(B) Extracts from transiently transfected HEK293T cells affinity purified against turboGFP shows C-terminal mutations interrupt endogenous FKBP8 and HSP90 binding to ZMYND10.
(C) Healthy human donor tracheal epithelial cultures (MucilAir) before ciliation (D17, post-ALI) or fully ciliated (D60, post-ALI), were cultured for 24 hours in control (vehicle only) or DM-CHX (concentrations indicated in µM) before harvesting protein extracts. Immature cultures (D17) were more sensitive to effects of specific PPIase inhibitor DM-CHX, destabilizing dynein components, whilst mature cultures were minimally affected.
(D) Quantification of band intensities for DNAH5 (blue) or DNAI1 (yellow) from (C) were normalized to loading control, and plotted as a fold change after 24 hours.
(E) Z projections of whole-mount immunofluorescence of mouse tracheal epithelial cultures (MTECs) stained with DNAH5 (magenta), DNAI2 (green) and DAPI (blue) after treatment of three days post-airlift (ALI) with either 100µm DM-CHX or vehicle control for 14 days in culture to differentiate, followed by switching cultures from control to 100µm DM-CHX (mature: cilial beat visualized) or from DM-CHX into vehicle control (no cilia beat) and culturing an additional 7 days. Treatment of mature ciliated cultures had little effect on DNAH5 and DNAI2 levels, whilst treatment during differentiation disrupted expression of dynein subunits, as evidenced by lack of axonemal staining in most cells (right panels) but release allows recovery of dynein pre-assembly, mostly cytoplasmic after 7 days.

Figure 8. ZMYND10 specifies dynein heavy chains as clients in a chaperone relay during dynein pre-assembly.

(A) Extracts from transiently transfected RPE-1 cells with ZMYND10-turboGFP variants and human LRRC6-myc were affinity purified against turboGFP (upper panels). Inclusion of LRRC6 destabilizes binding of wild-type ZMYND10 to endogenous FKBP8. C-terminal ZMYND10 mutations can interact with LRRC6. Expression of interactors is confirmed in input cell lysates (lower panels).
(B) During dynein arm assembly in the cytoplasm, ZMYND10 interaction with co-chaperone PPIase FKBP8 and HSP90 is required for the stabilization and folding of dynein heavy chains (DNAH). Competitive binding of LRRC6 to ZMYND10 likely advances the HSP90-FKBP8 chaperone cycle taking the client DNAHs to the next stage of assembly. We propose either R2TP or a specialized R2TP-like complex may function in parallel to assemble, scaffold or tether the DNAI1-DNAI2 heterodimeric complex via the PIH-domain proteins, such as DNAAF6, DNAAF2 and PIH1D2. The TPR-domain containing SPAG1 or DNAAF4 could recruit HSP90 via its MEEVD domain and together with RUVBL1/RUVBL2 these assembly factors could form a stable platform to promote HC-IC subunit interactions. This R2TP or R2TP-like complex likely operates distinctly to ZMYND10 as DNAI1/2 heterodimers are detected in *Zmynd10* mutants, however these are likely degraded if fully functional mature complexes (with heavy chains) cannot be assembled. This chaperone-relay system comprises several discrete chaperone complexes overseeing the folding and stability of discrete dynein subunits. Folding intermediates are handed off to successive complexes to promote stable interactions between subunits all the while preventing spurious interactions. Stable dynein complexes, once formed are targeted to cilia via transport adaptors and intraflagellar transport (IFT).

Source data: Figures 1-8- Uncropped immunoblots
Images show un-cropped versions of immunoblots. Figure panels used are demarcated with a box and the detected proteins are labeled. Asterisks are used to denote either non-specific bands (6C, 6D and 7B) or putative degradation products (7E). HE= High exposure, LE=Low exposure

Movie 1: Rapid ependymal ciliary motility in lateral ventricles of a wild-type mouse
High-speed video microscopy on a coronal brain vibratome section (postnatal day 11 mouse, littermate control) shows ependymal cilia lining lateral ventricles beating with high frequency in a wild-type mouse.

Movie 2: Immotile ependymal cilia lining lateral ventricles of *Zmynd10* mutant mouse
High-speed video microscopy on a coronal vibratome section of a brain from a *Zmynd10* mutant mouse (postnatal day 11) shows complete loss of ependymal cilia motility.

Movie 3: Control murine ependymal cilia with metachronal waveform
High-speed video microscopy on a coronal vibratome section of a *Zmynd10* mild hypomorphic mutant mouse brain (p. M179del; postnatal day 24) shows arrays of cilia beating in a metachronal waveform and actively generating fluid flow to move particulates over the ventricle tissue.

Movie 4: Tufts of immotile ependymal cilia in *Zmynd10* mutant murine brain
High-speed video microscopy on a coronal vibratome section of a *Zmynd10* null mutant mouse brain (p. L188del; postnatal day 29) shows arrays of immotile cilia lining the ventricle tissue with no active fluid flow noticeable.

Movie 5: Aberrant flagellar motility in ZMYND10 mutant murine epididymal spermatozoa
High-speed video microscopy on mature spermatozoa extracted from the epididymis of a 5 month old *Zmynd10* CRISPR founder mutant mouse and slowed-down in methylcellulose. The majority of spermatozoa were completely immotile but rarely displayed highly aberrant flagellar movements as observed in the video.

Movie 6: Sinusoidal flagellar motility in wild type murine epididymal spermatozoa

High-speed video microscopy on mature epididymal spermatozoa extracted from a 5 month-old wild-type mouse (littermate control) and slowed-down in methylcellulose. Virtually all spermatozoa underwent forward motion with the flagella displaying a sinusoidal beat pattern.

Supplementary File 1. Summary of label-free quantitative global proteomics of P25 testes from *Zmynd10*$^{+/+}$ and *Zmynd10*$^{-/-}$ mice. Label free quantitative (LFQ) proteomics were performed on whole testes extracts to compare differential protein expression profiles between *Zmynd10*$^{-/-}$ mutants and age matched (P25) wild-type littermate controls. LFQ intensities from three sets of biological replicates were averaged per genotype and ratios of enrichment or depletion in mutant versus wild type were calculated. Significance values were calculated using a Student's paired 2-tailed t-test. For ease of interpretation, the proteins were grouped into their respective complexes (i.e. Inner Dynein Arm Heavy Chains, Outer Dynein Arm Heavy Chains etc.)

Supplementary File 2. Endogenous ZMYND10 immunoprecipitation protein interactor profiling. Filtered by significance. Endogenous ZMYND10 was immunoprecipitated from total extracts of control wild type testes (P30) with two commercial polyclonal antibodies (Proteintech and Sigma). Proteins that co-precipitated with ZMYND10 in triplicate experiments were identified by tandem Mass Spectrometry and ranked according to fold-change (FC Ratio) enrichment and significance (t-test p-value) in the ZMYND10 specific pull-downs versus control immunoglobulin pull-downs. Proteins that commonly precipitated with ZMYND10 using the two separate polyclonal antibodies were considered putative interactors. A ranked list of these common hits is provided with ZMYND10 and the interactors investigated in this study i.e. FKBP8, HSP90AB1 and DNAH17 highlighted in green.

Supplementary File 3. Table of antibodies, qRT-PCR primers and plasmids used in this study.

Supplementary File 4. Table of additional mouse primers used in this study.

Materials and methods:

Key Resources Table

Reagent type (species) or resource	Designation	Source or reference	Identifiers	Additional information
gene (*Mus musculus*)	*Zmynd10*	NA	MGI:2387863; ENSMUSG00000010044;	Synonym: *Blu; Dnaaf7*
strain (*M. musculus*)	C57BL/6J	JAX	664	
strain (*M. musculus*)	C3H/HeJ	JAX	659	
strain (*M. musculus*)	CD1 (ICR)	Charles River	022	Outbred background
genetic reagent (*M. musculus*)	*Zmynd10*^{em1Pmi}	This paper	Allele symbol: *Zmynd10*^{em1Pmi}; Allele synonym: *Zmynd10*$^{-}$; Accession ID: MGI:TBC	CRISPR null allele of *Zmynd10; Zmynd10* c.695_701 p.Met178Ilefs*183
cell line (*H. sapiens*)	HEK 293	ATCC	CRL-1573	Human embryonic kidney cell line.
cell line (*H. sapiens*)	RPE-1	ATCC	CRL-4000	Human retinal pigmented epithelial cell line immortalized with hTERT.
biological sample (*M. musculus*)	mouse tracheal epithelial cells (mTECs)	This paper	NA	See Vladar and Brody, 2013 for protocol.
biological sample (*H. sapiens*)	MucilAir tracheal epithelial cell cultures	Epithelix Sarl	EP01MD	
antibody	Acetylated α-tubulin	Sigma	6-11B-1; T6793, RRID:AB_477585	IF (1:500-2000)
antibody	β-actin	Sigma	AC-15; A1978, RRID:AB_476692	WB (1:1000)
antibody	DNAAF1/LRRC50	Novus Biologicals	NBP2-01936; RRID: AB_2732031	WB (1:5000)
antibody	DNAH5	PMID: 23525783	Custom made	IF (1:100), PLA; WB (1:5000)
antibody	DNAH5	Sigma	HPA037470, RRID:AB_10672348	IF (1:100), PLA; WB (1:5000)
antibody	DNAH9	PMID: 24421334	Custom made	IF (1:100), PLA; WB (1:5000)
antibody	DNAH5	Sigma	HPA037470, RRID:AB_10672348	WB (1:5000)
antibody	DNAI1	Abcam	ab171964; RRID: AB_2732030	WB (1:5000)
antibody	DNAI2	Abnova	M01 clone IC8; H00064446-M01, RRID:AB_426059	IF (1:100), PLA; WB (1:5000)
antibody	DNAI2	Proteintech	17533-1-AP; 17533-1-AP, RRID:AB_2096670	IF (1:100); WB (1:5000); IP (1.5µg-3µg/IP)
antibody	DNALI1	Santa Cruz	N-13; sc-160296, RRID:AB_2246230	IF (1:75); WB (1:1000)
antibody	FKBP8	Proteintech	11173-1-AP, RRID:AB_10597097	WB (1:5000); IP (1.5µg-3µg/IP)
antibody	FKBP8	R&D Systems	MAB3580, RRID:AB_2262675	WB (1:5000)
antibody	γ tubulin	Abcam	GTU-88; ab11316, RRID:AB_297920	IF (1:500)
antibody	GAPDH	Abcam	ab8245, RRID:AB_2107448	WB (1:5000)
antibody	tGFP	Origene	TA150041, RRID:AB_2622256	IF (1:200); WB (1:5000)

antibody	GFP	Santa Cruz	FL; sc-8334, RRID:AB_641123	WB (1:5000); IP (1.5µg-3µg/IP)
antibody	GRP-94/HSP90B1	Thermo Scientific	clone 9G10; MA3-016, RRID:AB_2248666	IF (1:100); WB (1:5000)
antibody	HSP70	Santa Cruz	K-20; sc-1060, RRID:AB_631685	WB (1:5000)
antibody	HSP90AB1	R&D Systems	MAB32861, RRID:AB_2121071	WB (1:5000)
antibody	HSP90	Santa Cruz	Clone F-8; sc-13119, RRID:AB_675659	WB (1:5000)
antibody	LRRC6 (Hiroshi Hamada)	PMID:27353389	Custom made	WB (1:5000), a gift from Hiroshi Hamada
antibody	SENTAN	Sigma	HPA043322 , RRID: AB_10793945	IF (1:150)
antibody	ZMYND10	Proteintech	14431-1-AP, RRID:AB_2218002	WB (1:5000); IF (1:100); IP (1.5µg-3µg/IP)
antibody	ZMYND10	Sigma	HPA035255, RRID:AB_10601928	WB (1:5000); IF (1:100); IP (1.5µg-3µg/IP)
recombinant DNA reagent	*pCMV6-Zmynd10-tGFP*	Origene	MG207003	Mouse *Zmynd10* ORF with C-terminal turbo-GFP tag under CMV promoter in plasmid with ampicillin resistance gene
recombinant DNA reagent	*pCMV6-DNAAF5-tGFP*	Origene	MR221395	Mouse *Dnaaf5* ORF with C-terminal turbo-GFP tag under CMV promoter in plasmid with ampicillin resistance gene
recombinant DNA reagent	*pRK5-Myc-LRRC6*	PMID:23891469	NA	Human *LRRC6* ORF with myc tag; gift from the Hildebrandt and Gee labs
recombinant DNA reagent	*pX330-U6-Chimeric_BB-CBh-hSpCas9*	PMID: 23287718	Addgene:#42230	A human codon-optimized SpCas9 and chimeric guide RNA expression plasmid. pX330-U6-Chimeric_BB-CBh-hSpCas9 was a gift from Feng Zhang.
recombinant DNA reagent	*pCAG-EGxxFP*	PMID: 24284873	Addgene:#50716	5’ and 3’ EGFP fragments that shares 482bp were placed under ubiquitous CAG promoter. Used for validation of gRNA sequences by DSB mediated EGFP reconstitution. pCAG-EGxxFP was a gift from Masahito Ikawa
sequence-based reagent	mouse *Dnahc5* qRT-PCR primers	This paper		AAGCTGTTGCACCAGACCAT/ CCCAGGTGGCAGTTCTGTAG; Probe:88
sequence-based reagent	mouse *Dnali1* qRT-PCR primers	This paper		AGTTCCTGAAACGGACCAAC/ TGAGACCCATGTGGAAATGA; Probe:97
sequence-based reagent	mouse *Zmynd10* qRT-PCR primers	This paper		GCCATCCTTGATGCAACTATC/ CAATCAGCTCCTCCACCAG; Probe:64

sequence-based reagent	mouse *Tbp* qRT-PCR primers	This paper		GGGGAGCTGTGATGTGAAGT/ CCAGGAAATAATTCTGGCTCA; Probe:97
chemical compound, drug	N-(N'N'-Dimethylcarboxamidomethyl)cyclohexamide (DM-CHX)	PMID:16547004		FKBP8 inhibitor, 1mM stock in sterile PBS
software, algorithm	Fiji	PMID: 22743772		
software, algorithm	Nis-Elements AR V4.6	Nikon Instruments		
software, algorithm	Imaris V9.1	Bitplane		
software, algorithm	MaxQuant	PMID: 19029910		
software, algorithm	Andromeda	PMID: 21254760		
software, algorithm	Perseus	PMID: 27348712		
software, algorithm	Crapome	PMID: 23921808		

Generation of CRISPR mouse mutants

CAS9-mediated gene editing was used to generate mutant mice for *Zmynd10* (ENSEMBL:ENSMUSG00000010044) using three (guide) gRNAs each targeting "critical" exon 6. Guide RNA sequences were cloned into a pX330 vector (Addgene:#42230)(Cong et al., 2013) and efficacy was first validated using a split GFP assay in HEK293 cells (Addgene: #50716)(Mashiko et al., 2014). Pronuclear injections of 5ng/µl of purified plasmid DNA of pX330 constructs were injected into fertilized C57BL/6J eggs, which were cultured overnight until the two-cell stage before transferring to pseudopregnant females. PCR based screening, Sanger sequencing and characterization of genetic mutations of founder animals (F0) was performed. A genotyping was developed using a restriction digest of a PCR product for the -7bp deletion line used in this study. Animals were maintained in SPF environment and studies carried out under the guidance issued by the Medical Research Council in ''Responsibility in the Use of Animals in Medical Research'' (July 1993) and licensed by the Home Office under the Animals (Scientific Procedures) Act 1986.

Cytology, Histology and TEM

Motile multiciliated ependymal cells were obtained from mouse brains (>P7) using a published protocol(Grondona et al., 2013). Mouse respiratory epithelial cells were obtained by exposing the nasal septum and scraping cells off the epithelium with an interdental brush (TePe, 0.8mm ExtraSoft) followed by resuspension in DMEM (isolated from animals at P7-P29). Cells were spread on superfrost slides, air-dried and processed for immunofluorescence. This was modified for proximity ligation assay (PLA) where cells were resuspended in PBS, then fixed 4%PFA/3.7% sucrose/PBS for 30 minutes on ice and cytospun onto Superfrost slides. Human respiratory epithelial cells by brush biopsying the nasal epithelium of healthy human donors or P7 neonatal mice were processed for proximity ligation assay using a Duolink PLA starter kit (DUO92101, Sigma-Aldrich), as per the manufacturer's instructions following PFA fixation and 0.25%Triton-X100/TBS permeabilization 10 minutes. Alexa-488 phalloidin (Thermo Fischer) or rat anti-GRP94 (Thermo Fischer) counterstaining was done post-PLA protocol, prior to mounting in Duolink® In Situ Mounting Medium with DAPI (Sigma Aldrich). Trachea (P7), testes (P150) and oviducts (P7) were dissected and immersion fixed in 4% paraformaldehyde (from 16% solution, Thermo Fischer) overnight and

cryosectioned for immunofluorescence staining with antibodies to ZMYND10, acetylated α-tubulin or dynein components (Diggle et al., 2014). Nasal turbinates were similarly fixed and processed for paraffin sectioning stained with H&E to reveal mucus plugs. Immunofluorescence images were acquired at either 60x or 100x optical magnification as confocal stacks through whole cells and tissue sections using a Nikon A1R confocal microscope and displayed as Z-projections. Epididymal spermatozoa were isolated by dissecting the cauda and caput regions of the epididymides in M2 media (Life Technologies), spread onto superfrost slides and air-dried followed by fixation and permeabilisation for immunofluorescence, as previously described(Diggle et al., 2014). For counting, sperm from the cauda epididymides were immobilized by diluting in H_2O and counts were performed using a haemocytometer. For transmission electron microscopy, trachea tissue samples were dissected into PBS and immersion fixed in 2% PFA/2.5% glutaraldehyde (Sigma-Aldrich)/0.2M Sodium Cacodylate Buffer pH7.4 with 0.04% $CaCl_2$(Hall et al., 2013). Samples were cut into semi-thin and ultrathin sections and imaged by transmission electron microscopy (EM Services, Newcastle University Medical School).

Live brain sectioning and high-speed videomicroscopy of ependymal cilia

Whole brains were isolated from neonatal mice in ice cold PBS and kept on ice. Brains were mounted vertically along the caudo-rostral axis on a petri dish and embedded in low melting point agarose (Thermo Scientific). 400µm thick vibratome sections of live brain tissue were obtained and floated onto wells of a glass bottom multiwell plate (Greiner Sensoplates cat.662892) containing DMEM and maintained at 37°C and 5% CO_2. Sections were imaged on a Nikon macroscope to visualize dilated lateral ventricles. Motile cilia beating along the surfaces of the lateral walls were visualized and motility was recorded using a high-speed videomicroscopy Andor CCD camera attached to a confocal capture set-up.

Immunoprecipitations (IP) and immunoblots

Endogenous immunoprecipitations were performed using protein extracts either from multiciliated cell cultures or motile ciliated tissues lysed under mild lysis conditions (50 mM Tris-HCl (pH 7.5), 100 mM NaCl, 10% Glycerol, 0.5 mM EDTA, 0.5% IGEPAL, 0.15% Triton-X 100 and Halt Protease Inhibitor Single use cocktail EDTA free (Thermo Fischer)). For detecting HSP90 interactions, we included sodium molybdate (Sigma-Aldrich) in the IP buffer aiming to reduce ATP hydrolysis and client release(Sullivan et al., 2002). To detect interactions between ODA subunits, a DNAI2 antibody (Abnova H00064446-M01, RRID:AB_426059) was used as a bait to enrich DNAI2 containing complexes from mouse trachea and oviduct lysates. Immunoblotting was performed using DNAI1 (Abcam ab171964, RRID:AB_2732030) and DNAH5 (N-terminal epitope, M. Takeda). For ZMYND10 interaction studies, extracts from whole testes (P30) and differentiating mouse P7 oviducts were used. Endogenous ZMYND10 containing complexes were pulled out using two validated ZMYND10 polyclonal antibodies (Sigma HPA035255, RRID:AB_10601928; Proteintech 14431-1-AP, RRID:AB_2218002). Immunoblotting was performed using an HSP90 antibody (Santa Cruz sc-13119, RRID:AB_675659). For human samples, endogenous FKBP8, DNAI1 and DNAI2 pulldowns were perfomed on lysates from normal human airway epithelial cells (MucilAir, Epithelix Sarl) grown at air-liquid interface for 17days (immature cells). Antibodies for FKBP8 (Proteintech 11173-1-AP, RRID:AB_10597097), DNAI1 (Abcam ab171964; RRID:AB_2732030) and DNAI2 (Abnova H00064446-M01, RRID:AB_426059) were used as baits and antibodies for DNAH5 (Sigma HPA037470, RRID:AB_10672348) and ZMYND10 (Proteintech 14431-1-AP, RRID:AB_2218002) were used to detect these interactors. An isotype-matched IgG rabbit polyclonal antibody (GFP: sc-8334, RRID:AB_641123, Santa Cruz) was used as control. In all pull-down experiments, immunocomplexes were concentrated onto Protein G magnetic beads (PureProteome, Millipore). Following washes, immunocomplexes were eluted off the beads and resolved by SDS-PAGE for immunoblotting.

Alternatively, beads were processed for on-bead tryptic digestion and mass-spectrometric analysis. For overexpression pull-downs, of mouse *Dnaaf5-tGFP* (Origene- MG221395), *Zmynd10-tGFP* (Origene, MG207003) and *myc-Lrrc6* (Zariwala et al., 2013) were transiently transfected (Lipofectamine2000) into hTERT-RPE (ATCC CRL-4000) and HEK 293 (ATCC CRL-1573), which were tested regularly for mycoplasma. Site-directed mutagenesis was performed using two complementary PCR primers containing the desired nucleotide changes (PrimerX tool) to amplify *Zmynd10-tGFP* with proof reading DNA polymerase (Agilent II), followed by DpnI digestion, E coli transformation and sequencing of the thus recovered plasmids. Subsequent affinity purification using a turboGFP antibody (Evrogen TA150041, RRID:AB_2622256) was used to isolate fusion proteins 24 hours post-transfection followed by immobilization onto protein G beads. For immunoblots, proteins were resolved by SDS-PAGE using 3-8% Tris-Acetate gels or 4-12% Bis-Tris precast gels (NuPage Life Technologies), then transferred using XCell II Blot module (Life Technologies) to either nitrocellulose or PVDF membranes followed by manual or iBind Western (Thermo Fisher) system for antibody binding. Protein bands were detected using SuperSignal West Femto or Pico kit (Thermo Scientific). Supplementary File 3 contains a list of reagents used.

Mass Spectrometry and proteomic data analysis

For whole tissue proteome analysis, the Filter Aided Sample Preparation (FASP) method was used(Wiśniewski et al., 2009). Briefly, mouse testes samples were homogenized in a lysis buffer consisting of 100mM Tris (hydroxymethyl)amino-methane hydrochloride (Tris-HCl), pH 7.5, in presence of protease (Complete Mini Protease Inhibitor Tablets, Roche and 1mM Phenylmethylsulfonyl fluoride, , Sigma) and phosphatase inhibitors (PhosSTOP Phosphatase Inhibitor Cocktail Tablets, Roche). Samples were further processed and peptides and proteins were identified and quantified with the MaxQuant software package, and label-free quantification was performed by MaxLFQ, as described in (Hall et al., 2017). The false discovery rate, determined by searching a reverse database, was set at 0.01 for both peptides and proteins. All bioinformatic analyses were performed with the Perseus software. Intensity values were log-normalized, 0-values were imputed by a normal distribution 1.8 π down of the mean and with a width of 0.2 π. Statistically significant variance between the sample groups was tested by a permutation-based FDR approach and a Student's t test with a p value cut-off of 0.01. Total proteomic data are available via ProteomeXchange with identifier PXD006849 and are summarised in Supplementary File 1

To examine endogenous ZMYND10 interactions from postnatal day 30 (P30: a period of synchronized flagellogenesis) testes extracts using two well-validated polyclonal antibodies (ZMYND10 Proteintech and Sigma) using an IP/MS workflow carried according to (Turriziani et al., 2014). Mass spectra were analysed using MaxQuant software and label-free quantification intensity values were obtained for analysis. T-test p-values between MS runs were calculated. MS datasets were ranked by $\log_2$ fold-change (enrichment) over IgG controls (Supplementary File 2). As a filtering strategy to find 'true' interactions, we used the CRAPome repository (http://www.crapome.org/.) containing a comprehensive list of the most abundant contaminants commonly found in AP/MS experiments(Mellacheruvu et al., 2013). To aid filtering, we used an arbitrary threshold of 25 (i.e. proteins appearing in >25 out of 411 experiments captured in the CRAPome repository) were removed from further analysis. Filtered interactors common to both ranked datasets were prioritized for further studies for validation as interactors of ZMYND10 *in vivo*. The mass spectrometry proteomics data have been deposited to the ProteomeXchange Consortium via the PRIDE partner repository with the dataset identifier PXD006849 and summarised in Supplementary File 2.

Mouse tracheal epithelial cultures

Mouse tracheal epithelia cells (mTECs) were isolated from the tracheas of 5-7 week old outbred mice, and then studied as passage 0 cells(Vladar and Brody, 2013). Cells were cultured on semipermeable supported membranes (Transwell; Costar, Corning, NY), as previously described(Vladar and Brody, 2013). Y276342 (StemCell, UK) at 10 mM was added to the medium during the proliferation stages to promote basal cell proliferation. For FKBP8 inhibition studies, DM-CHX (1mM stock, in PBS) was diluted to 100µm working concentration in NuSerum media and added to wells every 2 days from 3 days ALI (immature treatment) or after 14 days (mature treatment). For detection of DNAH5 (Takeda custom) and DNAI2 (Abnova H00064446-M01, RRID:AB_426059) from mTECs, membrane from inserts were removed and stained with antibodies as described above.

Reverse transcription Quantitative Real time-PCR (RT qPCR)

Total RNA was isolated from freshly dissected tissue or tissue stored in RNAlater (Qiagen). Isolation was carried out using RNeasy Mini Kit or RNeasy Fibrous Tissue Mini Kit (Qiagen) following manufacturer's protocol. RNA samples were treated with Turbo DNAse to remove genomic DNA contamination using the Turbo DNA free kit (Ambion). Intron-spanning RT-qPCR assays were designed using the Universal Probe Library probe finder tool (Roche) to identify transcript specific primer-probe sets listed in supplementary table. Three separate experimental runs were carried out for each plate. All runs were done on three individual biological replicates. Data was analysed using Roche LC480 software. Subsequently, a paired two-tailed students t-test was used to compare differences in the mean expression values between wild type and mutant samples.

DM-CHX FKBP8 inhibitor studies

Lyophilized FKBP8 inhibitor N-(N'N'-Dimethylcarboxamidomethyl)cycloheximide (DM-CHX) (Edlich et al., 2006) was dissolved in sterile PBS in a 1mM stock and diluted further to working concentrations in MucilAir™ media (EPITHELIX Sàrl). MucilAir tracheal epithelial cultures (EPITHELIX Sàrl) inserts from healthy human donors (same for each stage, immature D17 after air-lift or mature D60 after air-lift) were incubated with DM-CHX for 24 hours and harvested in mild lysis buffer, (50 mM Tris-HCl (pH 7.5), 100 mM NaCl, 10% Glycerol, 0.5 mM EDTA, 0.5% IGEPAL, 0.15% Triton-X 100 and Halt Protease Inhibitor Single use cocktail EDTA free (Thermo Fischer).

Imaging

Fluorescent confocal images (PLA, IF, ICC) were acquired using a 60x Apochromat λS or 100x Plan Apochromat VC 1.4 DIC N2 lens was performed using a Nikon A1R confocal microscope. Data were acquired using NIS Elements AR software (Nikon Instruments Europe, Netherlands). mTEC wholemount images were acquired using 20x Plan Apochromat VC 0.75 DIC N2 or air 40x Plan Fluar 0.75 DIC N2 lens on the multimodal Imaging Platform Dragonfly (Andor Technologies, Belfast UK). Data were collected in Spinning Disk 25µm pinhole mode on the high sensitivity iXon888 EMCCD camera. Z stacks were collected using a Mad City Labs Piezo. Data was visualized using IMARIS 8.4 (Bitplane).

Statistics

Statistical tests were performed using GraphPad Prism 7, (GraphPad Software, California) as described in the text.

References

Back, R., Dominguez, C., Rothé, B., Bobo, C., Beaufils, C., Moréra, S., Meyer, P., Charpentier, B., Branlant, C., Allain, F.H.-T., Manival, X., 2013. High-resolution structural analysis shows how Tah1 tethers Hsp90 to the R2TP complex. Structure 21, 1834–1847. doi:10.1016/j.str.2013.07.024

Banasavadi-Siddegowda, Y.K., Mai, J., Fan, Y., Bhattacharya, S., Giovannucci, D.R., Sanchez, E.R., Fischer, G., Wang, X., 2011. FKBP38 peptidylprolyl isomerase promotes the folding of cystic fibrosis transmembrane conductance regulator in the endoplasmic reticulum. J. Biol. Chem. 286, 43071–43080. doi:10.1074/jbc.M111.269993

Barth, S., Edlich, F., Berchner-Pfannschmidt, U., Gneuss, S., Jahreis, G., Hasgall, P.A., Fandrey, J., Wenger, R.H., Camenisch, G., 2009. Hypoxia-inducible factor prolyl-4-hydroxylase PHD2 protein abundance depends on integral membrane anchoring of FKBP38. J. Biol. Chem. 284, 23046–23058. doi:10.1074/jbc.M109.032631

Barth, S., Nesper, J., Hasgall, P.A., Wirthner, R., Nytko, K.J., Edlich, F., Katschinski, D.M., Stiehl, D.P., Wenger, R.H., Camenisch, G., 2007. The peptidyl prolyl cis/trans isomerase FKBP38 determines hypoxia-inducible transcription factor prolyl-4-hydroxylase PHD2 protein stability. Mol. Cell. Biol. 27, 3758–3768. doi:10.1128/MCB.01324-06

Blundell, K.L.I.M., Pal, M., Roe, S.M., Pearl, L.H., Prodromou, C., 2017. The structure of FKBP38 in complex with the MEEVD tetratricopeptide binding-motif of Hsp90. PLOS ONE 12, e0173543. doi:10.1371/journal.pone.0173543

Cho, K.J., Noh, S.H., Han, S.M., Choi, W.-I., Kim, H.-Y., Yu, S., Lee, J.S., Rim, J.H., Lee, M.G., Hildebrandt, F., Gee, H.Y., 2018. ZMYND10 stabilizes intermediate chain proteins in the cytoplasmic pre-assembly of dynein arms. PLoS Genet. 14, e1007316. doi:10.1371/journal.pgen.1007316

Cong, L., Ran, F.A., Cox, D., Lin, S., Barretto, R., Habib, N., Hsu, P.D., Wu, X., Jiang, W., Marraffini, L.A., Zhang, F., 2013. Multiplex genome engineering using CRISPR/Cas systems. Science 339, 819–823. doi:10.1126/science.1231143

Desai, P.B., Dean, A.B., Mitchell, D.R., 2018. Cytoplasmic preassembly and trafficking of axonemal dyneins, in: Dyneins. Elsevier, pp. 140–161. doi:10.1016/B978-0-12-809471-6.00004-8

Diggle, C.P., Moore, D.J., Mali, G., Lage, zur, P., Ait-Lounis, A., Schmidts, M., Shoemark, A., Garcia Munoz, A., Halachev, M.R., Gautier, P., Yeyati, P.L., Bonthron, D.T., Carr, I.M., Hayward, B., Markham, A.F., Hope, J.E., Kriegsheim, von, A., Mitchison, H.M., Jackson, I.J., Durand, B., Reith, W., Sheridan, E., Jarman, A.P., Mill, P., 2014. HEATR2 plays a conserved role in assembly of the ciliary motile apparatus. PLoS Genet. 10, e1004577. doi:10.1371/journal.pgen.1004577

Dirksen, E.R., 1974. Ciliogenesis in the mouse oviduct. A scanning electron microscope study. J. Cell Biol. 62, 899–904.

Dong, F., Shinohara, K., Botilde, Y., Nabeshima, R., Asai, Y., Fukumoto, A., Hasegawa, T., Matsuo, M., Takeda, H., Shiratori, H., Nakamura, T., Hamada, H., 2014. Pih1d3 is required for cytoplasmic preassembly of axonemal dynein in mouse sperm. Journal of Cell Biology 204, 203–213. doi:10.1083/jcb.201304076

Dougherty, G.W., Loges, N.T., Klinkenbusch, J.A., Olbrich, H., Pennekamp, P., Menchen, T., Raidt, J., Wallmeier, J., Werner, C., Westermann, C., Ruckert, C., Mirra, V., Hjeij, R., Memari, Y., Durbin, R., Kolb-Kokocinski, A., Praveen, K., Kashef, M.A., Kashef, S., Eghtedari, F., Häffner, K., Valmari, P., Baktai, G., Aviram, M., Bentur, L., Amirav, I., Davis, E.E., Katsanis, N., Brueckner, M., Shaposhnykov, A., Pigino, G., Dworniczak, B., Omran, H., 2016. DNAH11 Localization in the Proximal Region of Respiratory Cilia Defines Distinct Outer Dynein Arm Complexes. Am. J. Respir. Cell Mol. Biol. 55, 213–224. doi:10.1165/rcmb.2015-0353OC

Edlich, F., Weiwad, M., Erdmann, F., Fanghänel, J., Jarczowski, F., Rahfeld, J.-U., Fischer, G., 2005. Bcl-2 regulator FKBP38 is activated by Ca2+/calmodulin. EMBO J. 24, 2688–2699. doi:10.1038/sj.emboj.7600739

Edlich, F., Weiwad, M., Wildemann, D., Jarczowski, F., Kilka, S., Moutty, M.-C., Jahreis, G., Lücke, C., Schmidt, W., Striggow, F., Fischer, G., 2006. The specific FKBP38 inhibitor N-(N“,N-

974 ”dimethylcarboxamidomethyl)cycloheximide has potent neuroprotective and neurotrophic
975 properties in brain ischemia. J. Biol. Chem. 281, 14961–14970. doi:10.1074/jbc.M600452200
976 Fliegauf, M., Olbrich, H., Horváth, J., Wildhaber, J.H., Zariwala, M.A., Kennedy, M., Knowles, M.R.,
977 Omran, H., 2005. Mislocalization of DNAH5 and DNAH9 in respiratory cells from patients with
978 primary ciliary dyskinesia. Am. J. Respir. Crit. Care Med. 171, 1343–1349.
979 doi:10.1164/rccm.200411-1583OC
980 Fok, A.K., Wang, H., Katayama, A., Aihara, M.S., Allen, R.D., 1994. 22S axonemal dynein is
981 preassembled and functional prior to being transported to and attached on the axonemes. Cell
982 Motil. Cytoskeleton 29, 215–224. doi:10.1002/cm.970290304
983 Fowkes, M.E., Mitchell, D.R., 1998. The role of preassembled cytoplasmic complexes in assembly of
984 flagellar dynein subunits. Mol. Biol. Cell 9, 2337–2347.
985 Grondona, J.M., Granados-Durán, P., Fernández-Llebrez, P., López-Ávalos, M.D., 2013. A simple
986 method to obtain pure cultures of multiciliated ependymal cells from adult rodents. Histochem.
987 Cell Biol. 139, 205–220. doi:10.1007/s00418-012-1008-2
988 Guichard, C., Harricane, M.C., Lafitte, J.J., Godard, P., Zaegel, M., Tack, V., Lalau, G., Bouvagnet, P.,
989 2001. Axonemal dynein intermediate-chain gene (DNAI1) mutations result in situs inversus and
990 primary ciliary dyskinesia (Kartagener syndrome). Am. J. Hum. Genet. 68, 1030–1035.
991 doi:10.1086/319511
992 Hall, E.A., Keighren, M., Ford, M.J., Davey, T., Jarman, A.P., Smith, L.B., Jackson, I.J., Mill, P., 2013.
993 Acute versus chronic loss of mammalian Azi1/Cep131 results in distinct ciliary phenotypes. PLoS
994 Genet. 9, e1003928. doi:10.1371/journal.pgen.1003928
995 Hall, E.A., Nahorski, M.S., Murray, L.M., Shaheen, R., Perkins, E., Dissanayake, K.N., Kristaryanto, Y.,
996 Jones, R.A., Vogt, J., Rivagorda, M., Handley, M.T., Mali, G.R., Quidwai, T., Soares, D.C., Keighren,
997 M.A., McKie, L., Mort, R.L., Gammoh, N., Garcia Munoz, A., Davey, T., Vermeren, M., Walsh, D.,
998 Budd, P., Aligianis, I.A., Faqeih, E., Quigley, A.J., Jackson, I.J., Kulathu, Y., Jackson, M., Ribchester,
999 R.R., Kriegsheim, von, A., Alkuraya, F.S., Woods, C.G., Maher, E.R., Mill, P., 2017. PLAA
1000 Mutations Cause a Lethal Infantile Epileptic Encephalopathy by Disrupting Ubiquitin-Mediated
1001 Endolysosomal Degradation of Synaptic Proteins. Am. J. Hum. Genet. 100, 706–724.
1002 doi:10.1016/j.ajhg.2017.03.008
1003 Huizar, R., Lee, C., Boulgakov, A., Horani, A., Tu, F., Drew, K., Marcotte, E., Brody, S., Wallingford, J.,
1004 2017. A phase separated organelle at the root of motile ciliopathy. doi:10.1101/213793
1005 Hutt, D.M., Roth, D.M., Chalfant, M.A., Youker, R.T., Matteson, J., Brodsky, J.L., Balch, W.E., 2012.
1006 FK506 binding protein 8 peptidylprolyl isomerase activity manages a late stage of cystic fibrosis
1007 transmembrane conductance regulator (CFTR) folding and stability. J. Biol. Chem. 287, 21914–
1008 21925. doi:10.1074/jbc.M112.339788
1009 Inaba, Y., Shinohara, K., Botilde, Y., Nabeshima, R., Takaoka, K., Ajima, R., Lamri, L., Takeda, H., Saga,
1010 Y., Nakamura, T., Hamada, H., 2016. Transport of the outer dynein arm complex to cilia requires
1011 a cytoplasmic protein Lrrc6. Genes Cells 21, 728–739. doi:10.1111/gtc.12380
1012 Jaffe, K.M., Grimes, D.T., Schottenfeld-Roames, J., Werner, M.E., Ku, T.-S.J., Kim, S.K., Pelliccia, J.L.,
1013 Morante, N.F.C., Mitchell, B.J., Burdine, R.D., 2016. c21orf59/kurly Controls Both Cilia Motility
1014 and Polarization. Cell Rep 14, 1841–1849. doi:10.1016/j.celrep.2016.01.069
1015 Kakihara, Y., Houry, W.A., 2012. The R2TP complex: discovery and functions. Biochim. Biophys. Acta
1016 1823, 101–107. doi:10.1016/j.bbamcr.2011.08.016
1017 Kobayashi, D., Asano-Hoshino, A., Nakakura, T., Nishimaki, T., Ansai, S., Kinoshita, M., Ogawa, M.,
1018 Hagiwara, H., Yokoyama, T., 2017. Loss of zinc finger MYND-type containing 10 (zmynd10)
1019 affects cilia integrity and axonemal localization of dynein arms, resulting in ciliary dysmotility,
1020 polycystic kidney and scoliosis in medaka (Oryzias latipes). Dev. Biol. 430, 69–79.
1021 doi:10.1016/j.ydbio.2017.08.016
1022 Kobayashi, D., Takeda, H., 2012. Ciliary motility: the components and cytoplasmic preassembly
1023 mechanisms of the axonemal dyneins. Differentiation 83, S23–9. doi:10.1016/j.diff.2011.11.009
1024 Kollmar, M., 2016. Fine-Tuning Motile Cilia and Flagella: Evolution of the Dynein Motor Proteins
1025 from Plants to Humans at High Resolution. Mol. Biol. Evol. 33, 3249–3267.
1026 doi:10.1093/molbev/msw213

Kott, E., Duquesnoy, P., Copin, B., Legendre, M., Dastot-Le Moal, F., Montantin, G., Jeanson, L., Tamalet, A., Papon, J.-F., Siffroi, J.-P., Rives, N., Mitchell, V., de Blic, J., Coste, A., Clement, A., Escalier, D., Touré, A., Escudier, E., Amselem, S., 2012. Loss-of-function mutations in LRRC6, a gene essential for proper axonemal assembly of inner and outer dynein arms, cause primary ciliary dyskinesia. Am. J. Hum. Genet. 91, 958–964. doi:10.1016/j.ajhg.2012.10.003

Kubo, A., Yuba-Kubo, A., Tsukita, S., Tsukita, S., Amagai, M., 2008. Sentan: a novel specific component of the apical structure of vertebrate motile cilia. Mol. Biol. Cell 19, 5338–5346. doi:10.1091/mbc.E08-07-0691

Kurkowiak, M., Ziętkiewicz, E., Greber, A., Voelkel, K., Wojda, A., Pogorzelski, A., Witt, M., 2016. ZMYND10 - Mutation Analysis in Slavic Patients with Primary Ciliary Dyskinesia. PLOS ONE 11, e0148067. doi:10.1371/journal.pone.0148067

Lage, zur, P., Stefanopoulou, P., Styczynska-Soczka, K., Quinn, N., Mali, G., Kriegsheim, von, A., Mill, P., Jarman, A.P., 2018. Ciliary dynein motor preassembly is regulated by Wdr92 in association with HSP90 co-chaperone, R2TP. J. Cell Biol. 3, jcb.201709026. doi:10.1083/jcb.201709026

Li, J., Buchner, J., 2013. Structure, function and regulation of the hsp90 machinery. Biomed J 36, 106–117. doi:10.4103/2319-4170.113230

Li, Y., Zhao, L., Yuan, S., Zhang, J., Sun, Z., 2017. Axonemal dynein assembly requires the R2TP complex component Pontin. Development dev.152314. doi:10.1242/dev.152314

Loges, N.T., Olbrich, H., Fenske, L., Mussaffi, H., Horváth, J., Fliegauf, M., Kuhl, H., Baktai, G., Peterffy, E., Chodhari, R., Chung, E.M.K., Rutman, A., O'Callaghan, C., Blau, H., Tiszlavicz, L., Voelkel, K., Witt, M., Ziętkiewicz, E., Neesen, J., Reinhardt, R., Mitchison, H.M., Omran, H., 2008. DNAI2 mutations cause primary ciliary dyskinesia with defects in the outer dynein arm. Am. J. Hum. Genet. 83, 547–558. doi:10.1016/j.ajhg.2008.10.001

Martino, F., Pal, M., Muñoz-Hernández, H., Rodríguez, C.F., Núñez-Ramírez, R., Gil-Carton, D., Degliesposti, G., Skehel, J.M., Roe, S.M., Prodromou, C., Pearl, L.H., Llorca, O., 2018. RPAP3 provides a flexible scaffold for coupling HSP90 to the human R2TP co-chaperone complex. Nat Commun 9, 1501. doi:10.1038/s41467-018-03942-1

Mashiko, D., Young, S.A.M., Muto, M., Kato, H., Nozawa, K., Ogawa, M., Noda, T., Kim, Y.-J., Satouh, Y., Fujihara, Y., Ikawa, M., 2014. Feasibility for a large scale mouse mutagenesis by injecting CRISPR/Cas plasmid into zygotes. Dev. Growth Differ. 56, 122–129. doi:10.1111/dgd.12113

Mellacheruvu, D., Wright, Z., Couzens, A.L., Lambert, J.-P., St-Denis, N.A., Li, T., Miteva, Y.V., Hauri, S., Sardiu, M.E., Low, T.Y., Halim, V.A., Bagshaw, R.D., Hubner, N.C., Al-Hakim, A., Bouchard, A., Faubert, D., Fermin, D., Dunham, W.H., Goudreault, M., Lin, Z.-Y., Badillo, B.G., Pawson, T., Durocher, D., Coulombe, B., Aebersold, R., Superti-Furga, G., Colinge, J., Heck, A.J.R., Choi, H., Gstaiger, M., Mohammed, S., Cristea, I.M., Bennett, K.L., Washburn, M.P., Raught, B., Ewing, R.M., Gingras, A.-C., Nesvizhskii, A.I., 2013. The CRAPome: a contaminant repository for affinity purification-mass spectrometry data. Nat. Methods 10, 730–736. doi:10.1038/nmeth.2557

Mitchison, H.M., Schmidts, M., Loges, N.T., Freshour, J., Dritsoula, A., Hirst, R.A., O'Callaghan, C., Blau, H., Dabbagh, Al, M., Olbrich, H., Beales, P.L., Yagi, T., Mussaffi, H., Chung, E.M.K., Omran, H., Mitchell, D.R., 2012. Mutations in axonemal dynein assembly factor DNAAF3 cause primary ciliary dyskinesia. Nat. Genet. 44, 381–9– S1–2. doi:10.1038/ng.1106

Moore, D.J., Onoufriadis, A., Shoemark, A., Simpson, M.A., Lage, zur, P.I., de Castro, S.C., Bartoloni, L., Gallone, G., Petridi, S., Woollard, W.J., Antony, D., Schmidts, M., Didonna, T., Makrythanasis, P., Bevillard, J., Mongan, N.P., Djakow, J., Pals, G., Lucas, J.S., Marthin, J.K., Nielsen, K.G., Santoni, F., Guipponi, M., Hogg, C., Antonarakis, S.E., Emes, R.D., Chung, E.M.K., Greene, N.D.E., Blouin, J.-L., Jarman, A.P., Mitchison, H.M., 2013. Mutations in ZMYND10, a gene essential for proper axonemal assembly of inner and outer dynein arms in humans and flies, cause primary ciliary dyskinesia. Am. J. Hum. Genet. 93, 346–356. doi:10.1016/j.ajhg.2013.07.009

Morgen, von, P., Hořejší, Z., Macurek, L., 2015. Substrate recognition and function of the R2TP complex in response to cellular stress. Front Genet 6, 69. doi:10.3389/fgene.2015.00069

Nakagawa, T., Shirane, M., Iemura, S.-I., Natsume, T., Nakayama, K.I., 2007. Anchoring of the 26S proteasome to the organellar membrane by FKBP38. Genes Cells 12, 709–719. doi:10.1111/j.1365-2443.2007.01086.x

Olbrich, H., Häffner, K., Kispert, A., Völkel, A., Volz, A., Sasmaz, G., Reinhardt, R., Hennig, S., Lehrach, H., Konietzko, N., Zariwala, M., Noone, P.G., Knowles, M., Mitchison, H.M., Meeks, M., Chung, E.M.K., Hildebrandt, F., Sudbrak, R., Omran, H., 2002. Mutations in DNAH5 cause primary ciliary dyskinesia and randomization of left-right asymmetry. Nat. Genet. 30, 143–144. doi:10.1038/ng817

Olcese, C., Patel, M.P., Shoemark, A., Kiviluoto, S., Legendre, M., Williams, H.J., Vaughan, C.K., Hayward, J., Goldenberg, A., Emes, R.D., Munye, M.M., Dyer, L., Cahill, T., Bevillard, J., Gehrig, C., Guipponi, M., Chantot, S., Duquesnoy, P., Thomas, L., Jeanson, L., Copin, B., Tamalet, A., Thauvin-Robinet, C., Papon, J.-F., Garin, A., Pin, I., Vera, G., Aurora, P., Fassad, M.R., Jenkins, L., Boustred, C., Cullup, T., Dixon, M., Onoufriadis, A., Bush, A., Chung, E.M.K., Antonarakis, S.E., Loebinger, M.R., Wilson, R., Armengot, M., Escudier, E., Hogg, C., Amselem, S., Sun, Z., Bartoloni, L., Blouin, J.-L., Mitchison, H.M., 2017. X-linked primary ciliary dyskinesia due to mutations in the cytoplasmic axonemal dynein assembly factor PIH1D3. Nat Commun 8, 14279. doi:10.1038/ncomms14279

Omran, H., Kobayashi, D., Olbrich, H., Tsukahara, T., Loges, N.T., Hagiwara, H., Zhang, Q., Leblond, G., O'Toole, E., Hara, C., Mizuno, H., Kawano, H., Fliegauf, M., Yagi, T., Koshida, S., Miyawaki, A., Zentgraf, H., Seithe, H., Reinhardt, R., Watanabe, Y., Kamiya, R., Mitchell, D.R., Takeda, H., 2008. Ktu/PF13 is required for cytoplasmic pre-assembly of axonemal dyneins. Nature 456, 611–616. doi:10.1038/nature07471

Paff, T., Loges, N.T., Aprea, I., Wu, K., Bakey, Z., Haarman, E.G., Daniels, J.M.A., Sistermans, E.A., Bogunovic, N., Dougherty, G.W., Höben, I.M., Große-Onnebrink, J., Matter, A., Olbrich, H., Werner, C., Pals, G., Schmidts, M., Omran, H., Micha, D., 2017. Mutations in PIH1D3 Cause X-Linked Primary Ciliary Dyskinesia with Outer and Inner Dynein Arm Defects. Am. J. Hum. Genet. 100, 160–168. doi:10.1016/j.ajhg.2016.11.019

Pal, M., Morgan, M., Phelps, S.E.L., Roe, S.M., Parry-Morris, S., Downs, J.A., Polier, S., Pearl, L.H., Prodromou, C., 2014. Structural basis for phosphorylation-dependent recruitment of Tel2 to Hsp90 by Pih1. Structure 22, 805–818. doi:10.1016/j.str.2014.04.001

Pennarun, G., Escudier, E., Chapelin, C., Bridoux, A.M., Cacheux, V., Roger, G., Clément, A., Goossens, M., Amselem, S., Duriez, B., 1999. Loss-of-function mutations in a human gene related to Chlamydomonas reinhardtii dynein IC78 result in primary ciliary dyskinesia. Am. J. Hum. Genet. 65, 1508–1519. doi:10.1086/302683

Qin, H., Diener, D.R., Geimer, S., Cole, D.G., Rosenbaum, J.L., 2004. Intraflagellar transport (IFT) cargo: IFT transports flagellar precursors to the tip and turnover products to the cell body. J. Cell Biol. 164, 255–266. doi:10.1083/jcb.200308132

Saita, S., Shirane, M., Ishitani, T., Shimizu, N., Nakayama, K.I., 2014. Role of the ANKMY2-FKBP38 axis in regulation of the Sonic hedgehog (Shh) signaling pathway. J. Biol. Chem. 289, 25639–25654. doi:10.1074/jbc.M114.558635

Sullivan, W.P., Owen, B.A.L., Toft, D.O., 2002. The influence of ATP and p23 on the conformation of hsp90. J. Biol. Chem. 277, 45942–45948. doi:10.1074/jbc.M207754200

Taipale, M., Tucker, G., Peng, J., Krykbaeva, I., Lin, Z.-Y., Larsen, B., Choi, H., Berger, B., Gingras, A.-C., Lindquist, S., 2014. A quantitative chaperone interaction network reveals the architecture of cellular protein homeostasis pathways. Cell 158, 434–448. doi:10.1016/j.cell.2014.05.039

Tarkar, A., Loges, N.T., Slagle, C.E., Francis, R., Dougherty, G.W., Tamayo, J.V., Shook, B., Cantino, M., Schwartz, D., Jahnke, C., Olbrich, H., Werner, C., Raidt, J., Pennekamp, P., Abouhamed, M., Hjeij, R., Köhler, G., Griese, M., Li, Y., Lemke, K., Klena, N., Liu, X., Gabriel, G., Tobita, K., Jaspers, M., Morgan, L.C., Shapiro, A.J., Letteboer, S.J.F., Mans, D.A., Carson, J.L., Leigh, M.W., Wolf, W.E., Chen, S., Lucas, J.S., Onoufriadis, A., Plagnol, V., Schmidts, M., Boldt, K., UK10K, Roepman, R., Zariwala, M.A., Lo, C.W., Mitchison, H.M., Knowles, M.R., Burdine, R.D., Loturco, J.J., Omran, H., 2013. DYX1C1 is required for axonemal dynein assembly and ciliary motility. Nat. Genet. 45, 995–1003. doi:10.1038/ng.2707

Turriziani, B., Garcia Munoz, A., Pilkington, R., Raso, C., Kolch, W., Kriegsheim, von, A., 2014. On-beads digestion in conjunction with data-dependent mass spectrometry: a shortcut to quantitative and dynamic interaction proteomics. Biology (Basel) 3, 320–332.

doi:10.3390/biology3020320
Vladar, E.K., Brody, S.L., 2013. Analysis of Ciliogenesis in Primary Culture Mouse Tracheal Epithelial Cells, in: Cilia, Part B, Methods in Enzymology. Elsevier, pp. 285–309. doi:10.1016/B978-0-12-397944-5.00014-6
Wang, X., Venable, J., LaPointe, P., Hutt, D.M., Koulov, A.V., Coppinger, J., Gurkan, C., Kellner, W., Matteson, J., Plutner, H., Riordan, J.R., Kelly, J.W., Yates, J.R., Balch, W.E., 2006. Hsp90 cochaperone Aha1 downregulation rescues misfolding of CFTR in cystic fibrosis. Cell 127, 803–815. doi:10.1016/j.cell.2006.09.043
Wickstead, B., Gull, K., 2007. Dyneins across eukaryotes: a comparative genomic analysis. Traffic 8, 1708–1721. doi:10.1111/j.1600-0854.2007.00646.x
Wiśniewski, J.R., Zougman, A., Nagaraj, N., Mann, M., 2009. Universal sample preparation method for proteome analysis. Nat. Methods 6, 359–362. doi:10.1038/nmeth.1322
Yamaguchi, H., Oda, T., Kikkawa, M., Takeda, H., 2018. Systematic studies of all PIH proteins in zebrafish reveal their distinct roles in axonemal dynein assembly. eLife 7, e36979. doi:10.7554/eLife.36979
Zariwala, M.A., Gee, H.Y., Kurkowiak, M., Al-Mutairi, D.A., Leigh, M.W., Hurd, T.W., Hjeij, R., Dell, S.D., Chaki, M., Dougherty, G.W., Adan, M., Spear, P.C., Esteve-Rudd, J., Loges, N.T., Rosenfeld, M., Diaz, K.A., Olbrich, H., Wolf, W.E., Sheridan, E., Batten, T.F.C., Halbritter, J., Porath, J.D., Kohl, S., Lovric, S., Hwang, D.-Y., Pittman, J.E., Burns, K.A., Ferkol, T.W., Sagel, S.D., Olivier, K.N., Morgan, L.C., Werner, C., Raidt, J., Pennekamp, P., Sun, Z., Zhou, W., Airik, R., Natarajan, S., Allen, S.J., Amirav, I., Wieczorek, D., Landwehr, K., Nielsen, K., Schwerk, N., Sertic, J., Köhler, G., Washburn, J., Levy, S., Fan, S., Koerner-Rettberg, C., Amselem, S., Williams, D.S., Mitchell, B.J., Drummond, I.A., Otto, E.A., Omran, H., Knowles, M.R., Hildebrandt, F., 2013. ZMYND10 is mutated in primary ciliary dyskinesia and interacts with LRRC6. Am. J. Hum. Genet. 93, 336–345. doi:10.1016/j.ajhg.2013.06.007

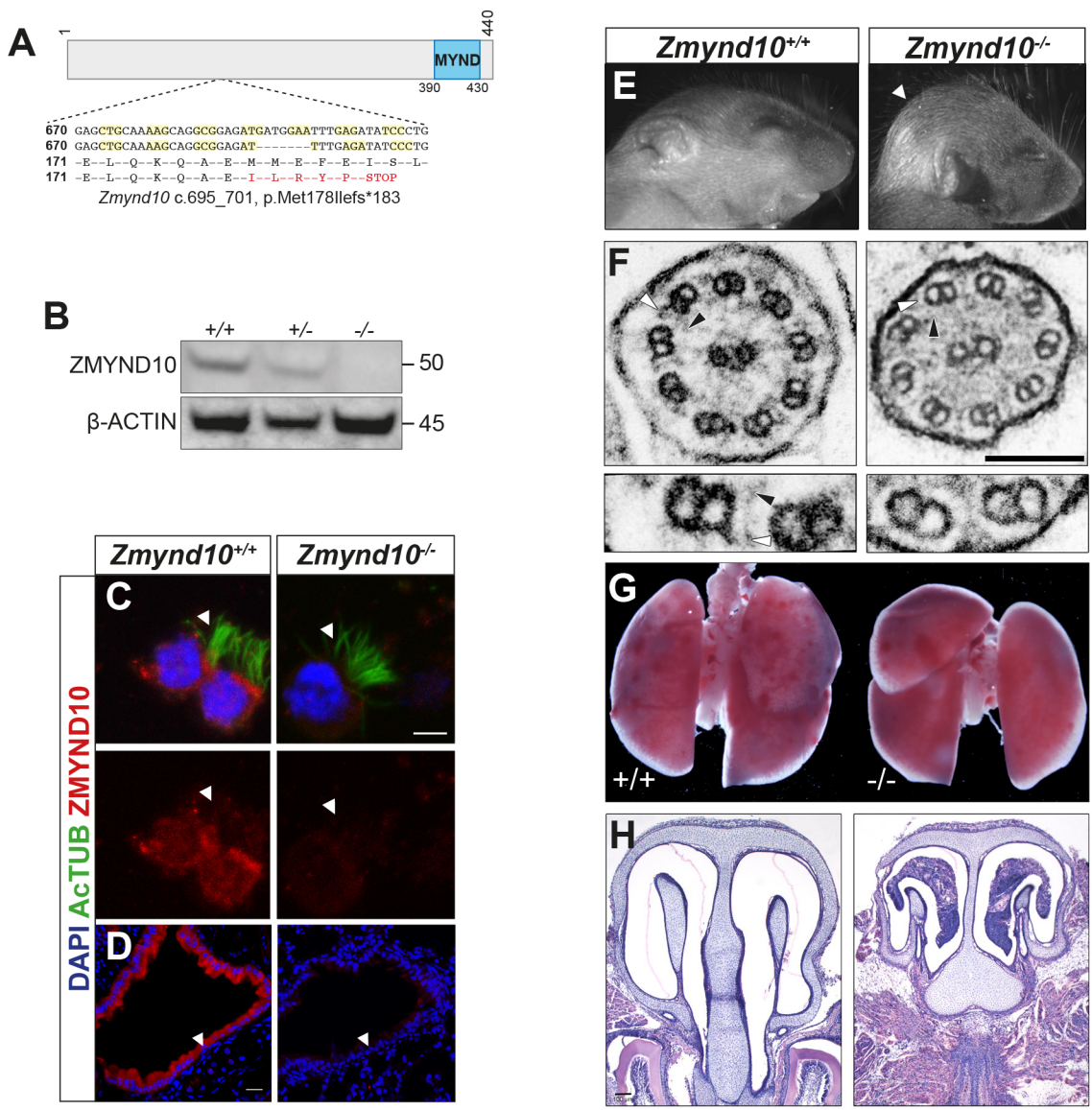
A
1
440
MYND
390
430
670 GAGCTGCAAAAGCAGGCGGAGATGATGGAATTTGAGATATCCCTG
670 GAGCTGCAAAAGCAGGCGGAGAT-------TTTGAGATATCCCTG
171 -E--L--Q--K--Q--A--E--M--M--E--F--E--I--S--L-
171 -E--L--Q--K--Q--A--E--I--L--R--Y--P--STOP
Zmynd10 c.695_701, p.Met178Ilefs*183
B
+/+
+/-
-/-
ZMYND10
50
β-ACTIN
45
Zmynd10+/+
Zmynd10-/-
C
D
DAPI AcTUB ZMYND10
E
F
G
+/+
-/-
H

A

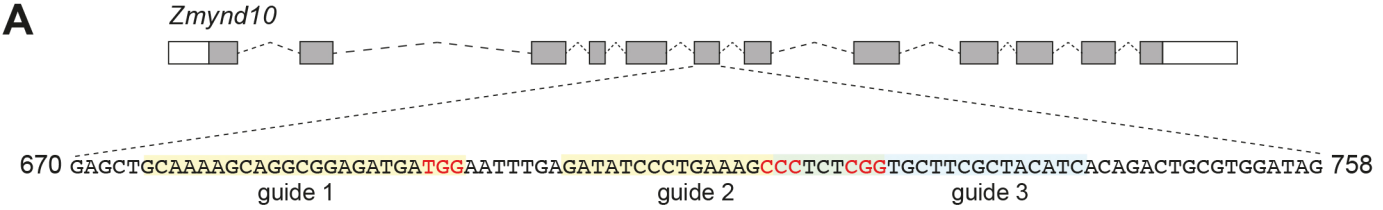

B

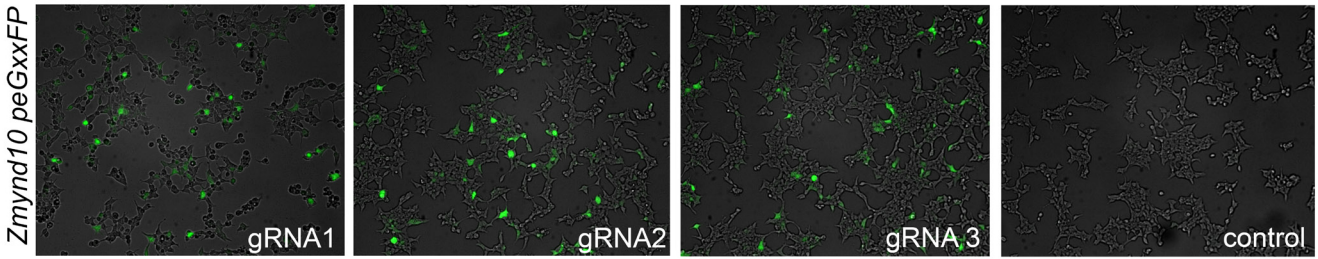

C

Zmynd10 gRNA	No. injections	No. injected	No. 2 cell	No. born	No. weaning	Cas9+	Edited	Mutation type	GLT?
1	1	82	52	6	6	0/6	4/6	Compound deletions and insertions: +1bp, -3bp, -6bp, -7bp, -8bp, -23bp	Yes
2	2	177	112	6	6	1/6	1/6	Compound deletions: -19bp, -23bp	Yes
		173	114	30	28	1/28	6/28	Compound deletions: -2bp, -3bp,-4bp, -5bp	Yes
3	1	179	138	29	27	0/27	11/27	Compound deletiona and insertions: +1bp, -1bp, -3bp, -9bp, -11bp, -28bp	Yes

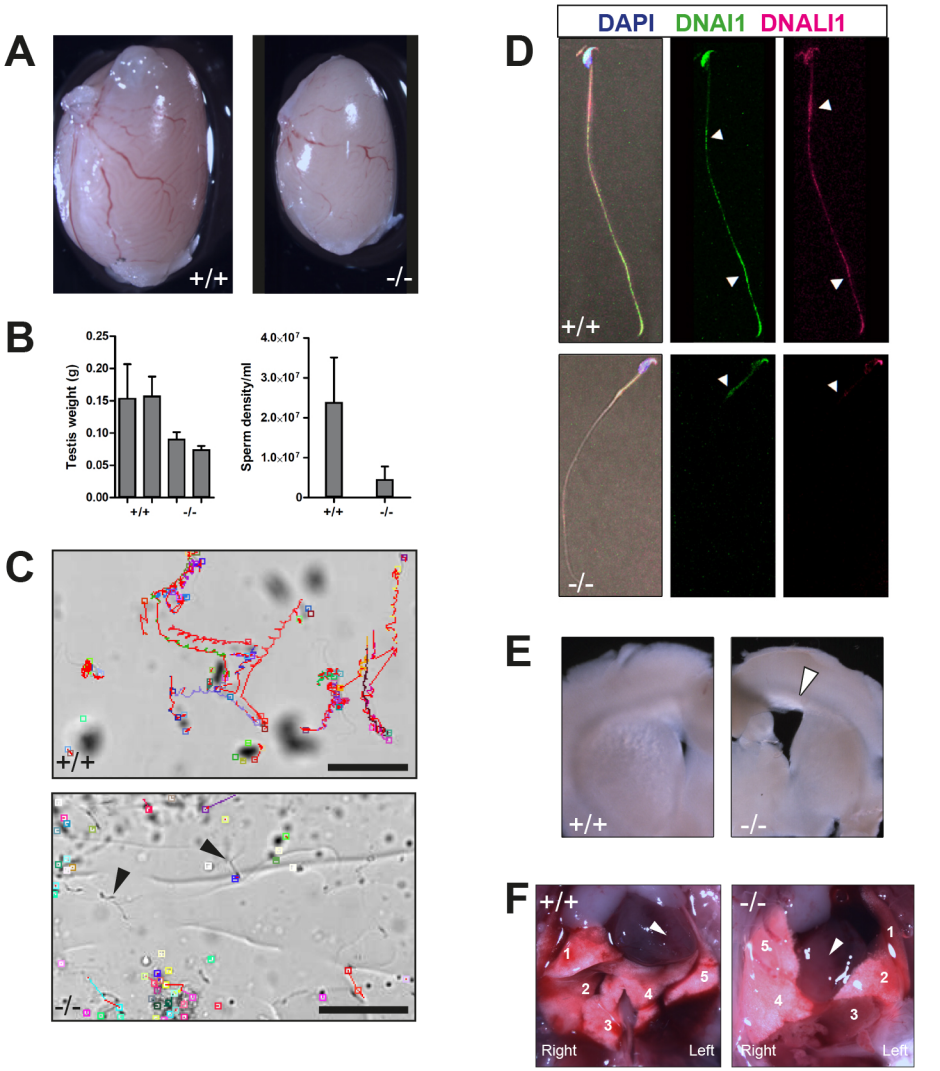
A
+/+
-/-
B
Testis weight (g)
0.25
0.20
0.15
0.10
0.05
0.00
+/+
-/-
Sperm density/ml
4.0x10^7
3.0x10^7
2.0x10^7
1.0x10^7
0
+/+
-/-
C
+/+
-/-
D
DAPI
DNAI1
DNALI1
+/+
-/-
E
+/+
-/-
F
+/+
1
2
3
4
5
Right
Left
-/-
1
2
3
4
5
Right
Left

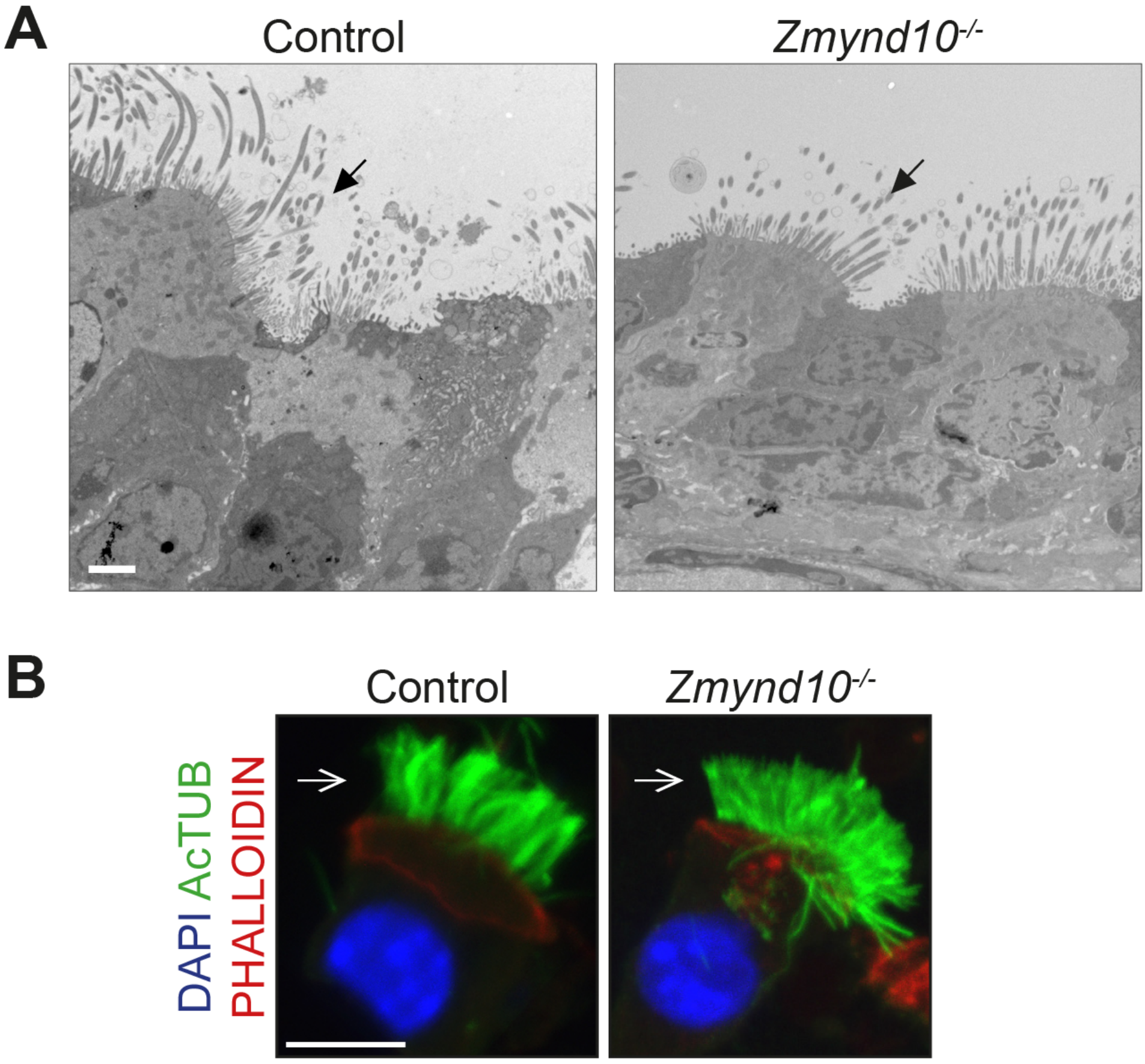
A
Control
Zmynd10-/-
B
Control
Zmynd10-/-
DAPI AcTUB
PHALLOIDIN

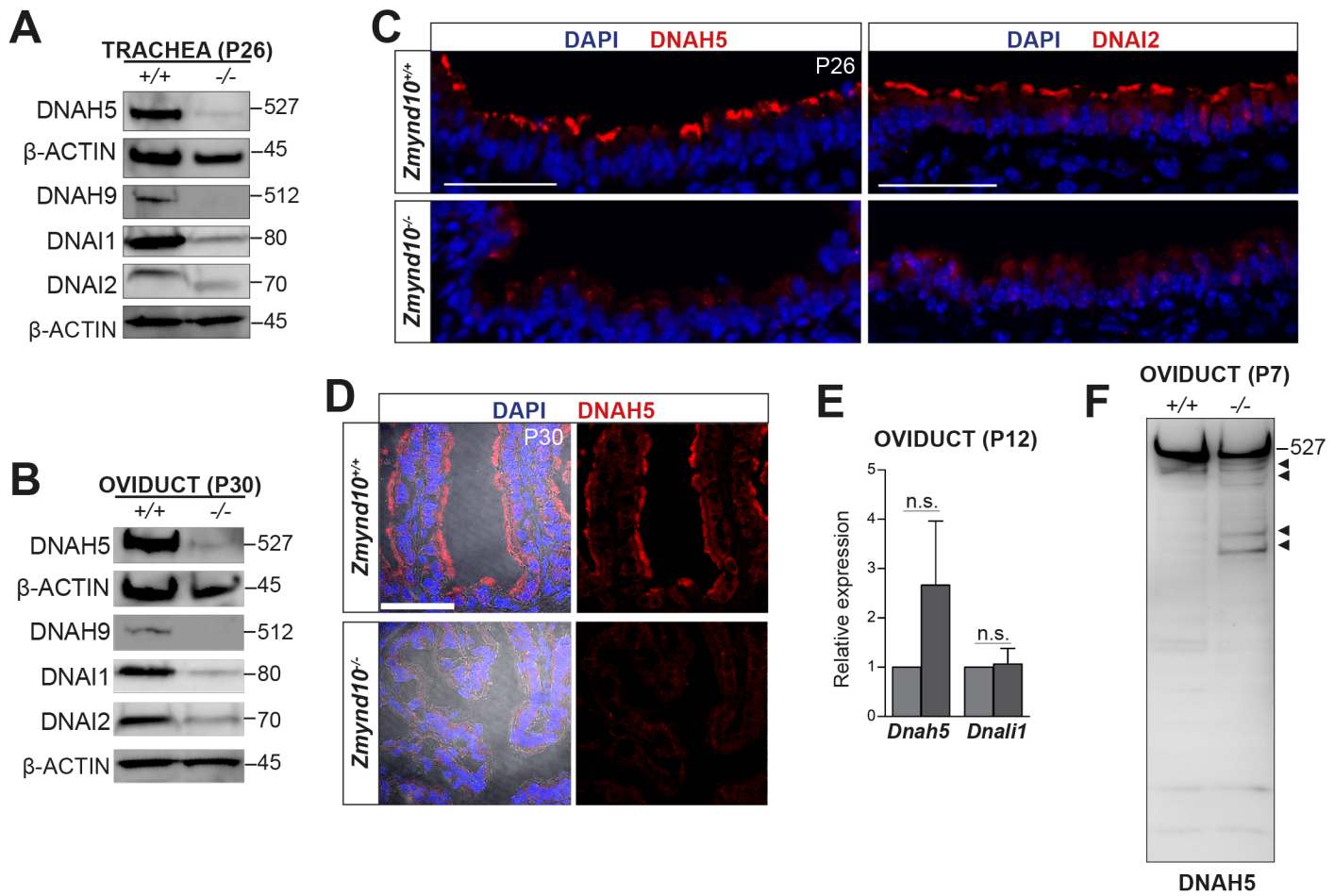
A
TRACHEA (P26)
+/+
-/-
DNAH5
β-ACTIN
DNAH9
DNAI1
DNAI2
β-ACTIN
527
45
512
80
70
45
B
OVIDUCT (P30)
+/+
-/-
DNAH5
β-ACTIN
DNAH9
DNAI1
DNAI2
β-ACTIN
527
45
512
80
70
45
C
DAPI
DNAH5
P26
DAPI
DNAI2
Zmynd10+/+
Zmynd10-/-
D
DAPI
DNAH5
P30
Zmynd10+/+
Zmynd10-/-
E
OVIDUCT (P12)
Relative expression
n.s.
n.s.
Dnah5
Dnali1
F
OVIDUCT (P7)
+/+
-/-
527
DNAH5

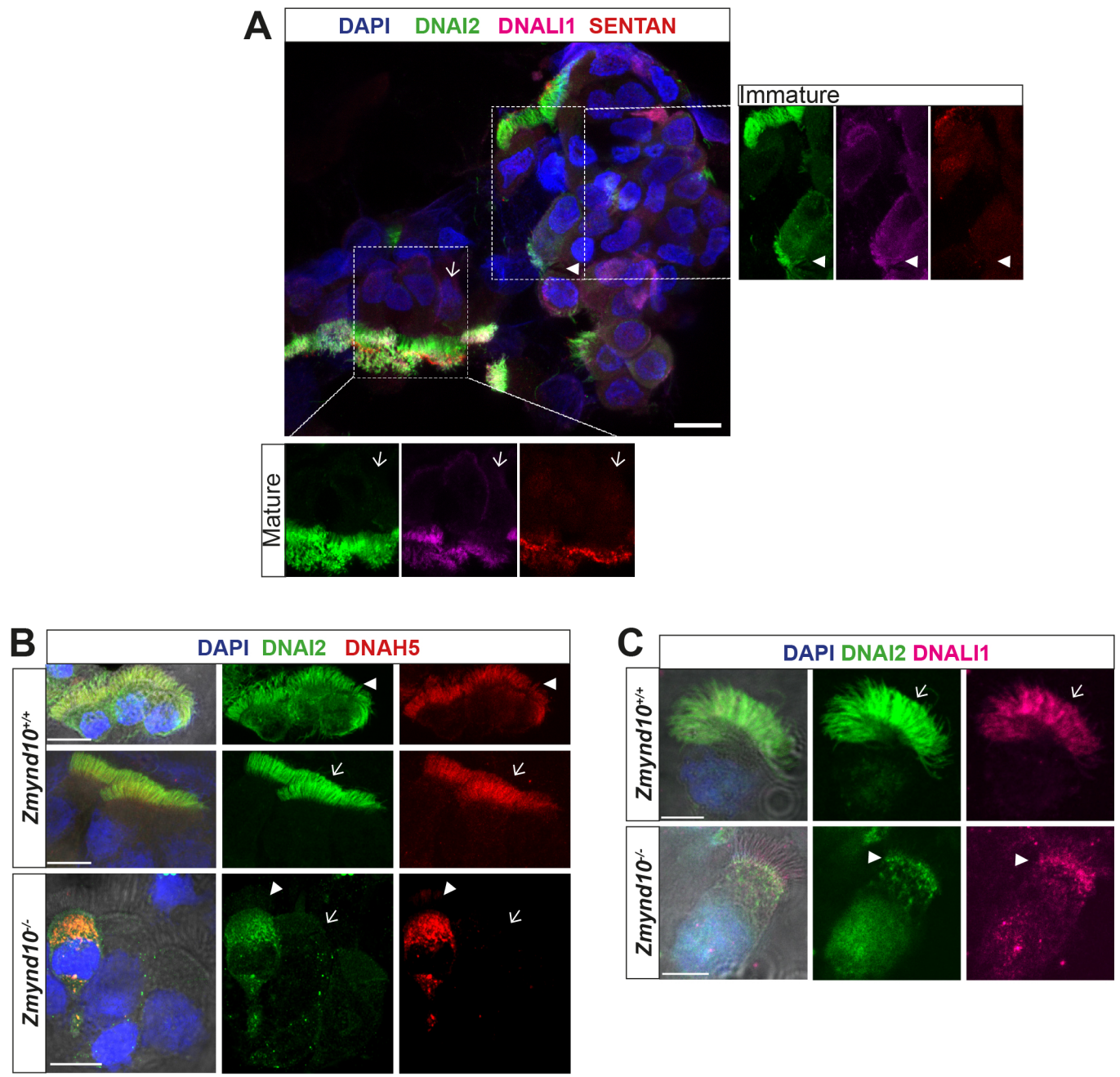
A
DAPI DNAI2 DNALI1 SENTAN
Immature
Mature
B
DAPI DNAI2 DNAH5
Zmynd10+/+
Zmynd10-/-
C
DAPI DNAI2 DNALI1
Zmynd10+/+
Zmynd10-/-

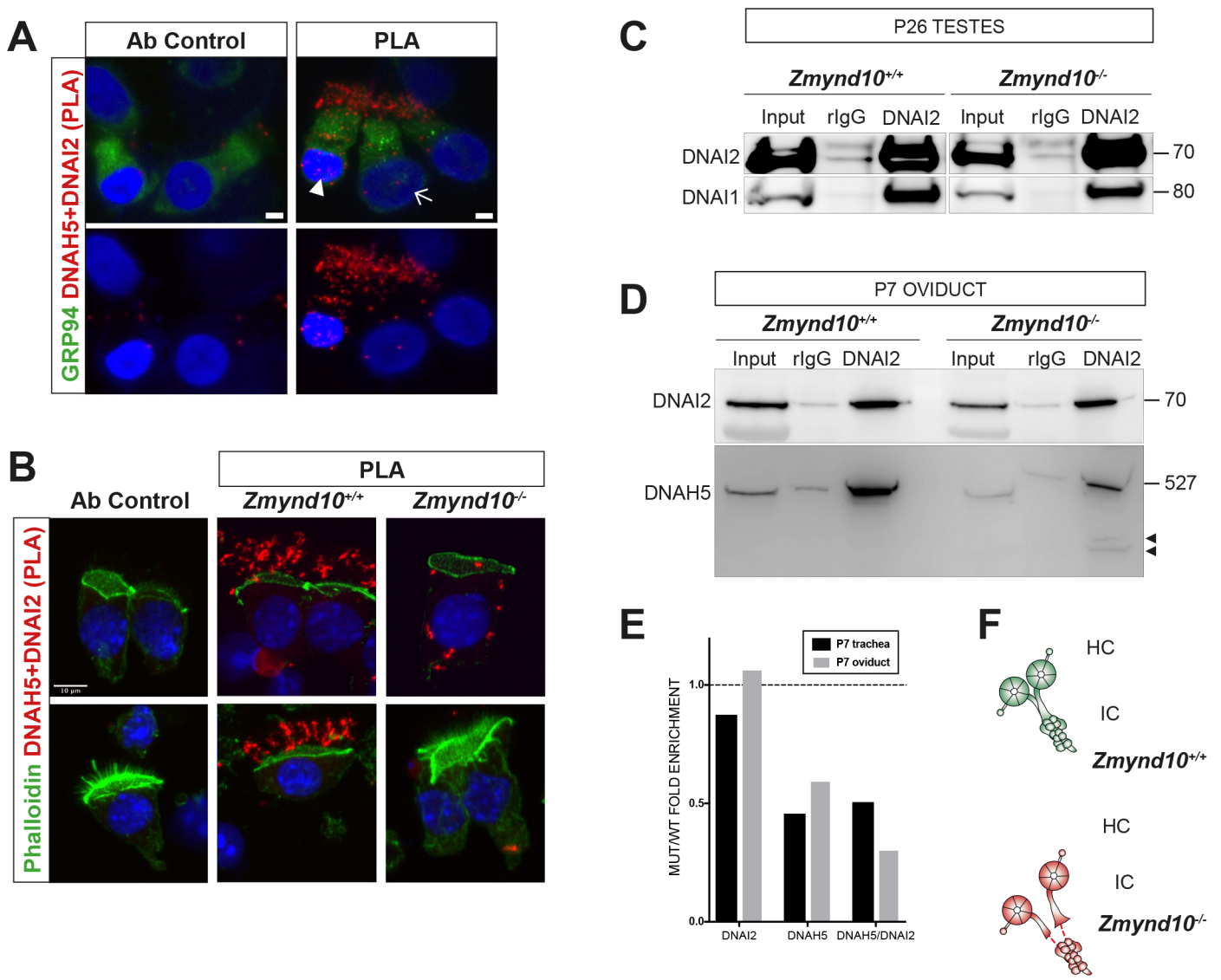
A
Ab Control
PLA
GRP94 DNAH5+DNAI2 (PLA)
B
Ab Control
PLA
Zmynd10+/+
Zmynd10-/-
Phalloidin DNAH5+DNAI2 (PLA)
10 µm
C
P26 TESTES
Zmynd10+/+
Zmynd10-/-
Input
rIgG
DNAI2
DNAI2
DNAI1
70
80
D
P7 OVIDUCT
Zmynd10+/+
Zmynd10-/-
Input
rIgG
DNAI2
DNAH5
70
527
E
P7 trachea
P7 oviduct
MUT/WT FOLD ENRICHMENT
1.0
0.5
0.0
DNAI2
DNAH5
DNAH5/DNAI2
F
HC
IC
Zmynd10+/+
HC
IC
Zmynd10-/-

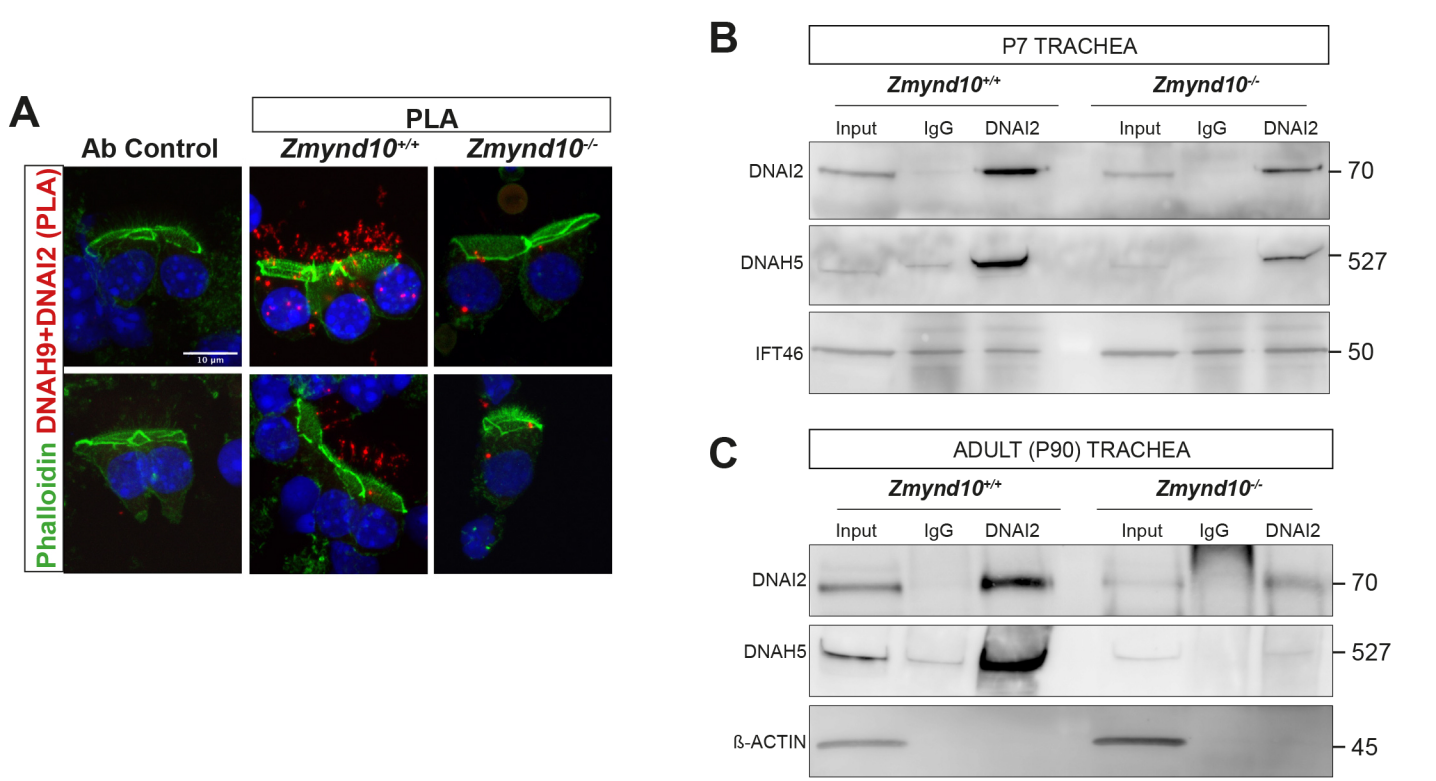
A
PLA
Ab Control
Zmynd10+/+
Zmynd10-/-
Phalloidin DNAH9+DNAI2 (PLA)
10 µm
B
P7 TRACHEA
Zmynd10+/+
Zmynd10-/-
Input
IgG
DNAI2
Input
IgG
DNAI2
DNAI2
DNAH5
IFT46
70
527
50
C
ADULT (P90) TRACHEA
Zmynd10+/+
Zmynd10-/-
Input
IgG
DNAI2
Input
IgG
DNAI2
DNAI2
DNAH5
ß-ACTIN
70
527
45

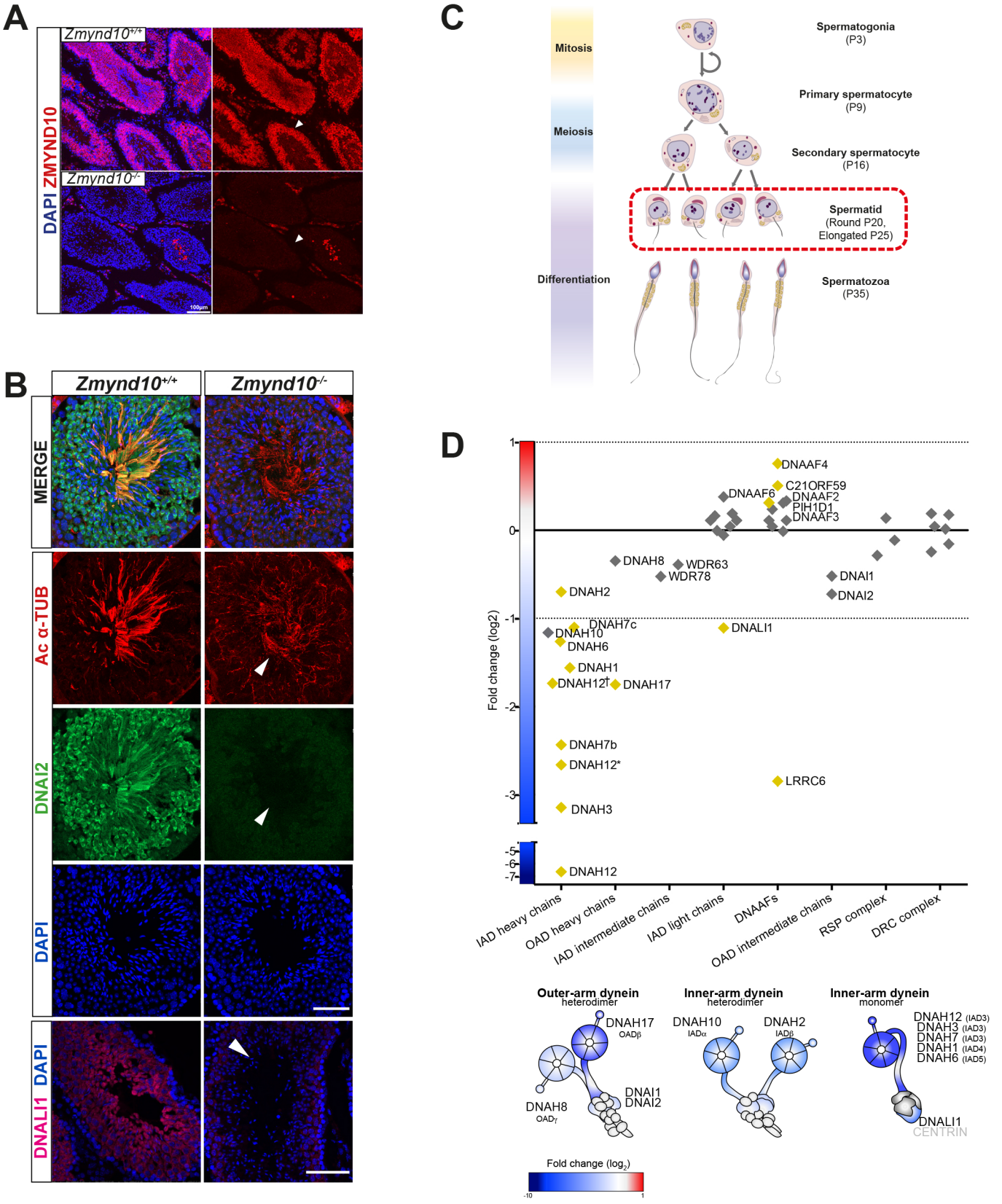
A
Zmynd10+/+
Zmynd10-/-
DAPI ZMYND10
100µm
B
Zmynd10+/+
Zmynd10-/-
MERGE
Ac α-TUB
DNAI2
DAPI
DNALI1 DAPI
C
Mitosis
Meiosis
Differentiation
Spermatogonia
(P3)
Primary spermatocyte
(P9)
Secondary spermatocyte
(P16)
Spermatid
(Round P20,
Elongated P25)
Spermatozoa
(P35)
D
Fold change (log2)
DNAAF4
C21ORF59
DNAAF6
DNAAF2
PIH1D1
DNAAF3
DNAH8
WDR63
WDR78
DNAI1
DNAI2
DNAH2
DNAH7c
DNALI1
DNAH10
DNAH6
DNAH1
DNAH12†
DNAH17
DNAH7b
DNAH12*
LRRC6
DNAH3
DNAH12
IAD heavy chains
OAD heavy chains
IAD intermediate chains
IAD light chains
DNAAFs
OAD intermediate chains
RSP complex
DRC complex
Outer-arm dynein
heterodimer
DNAH17
OADβ
DNAI1
DNAI2
DNAH8
OADγ
Inner-arm dynein
heterodimer
DNAH10
IADα
DNAH2
IADβ
Inner-arm dynein
monomer
DNAH12 (IAD3)
DNAH3 (IAD3)
DNAH7 (IAD3)
DNAH1 (IAD4)
DNAH6 (IAD5)
DNALI1
CENTRIN
Fold change (log2)

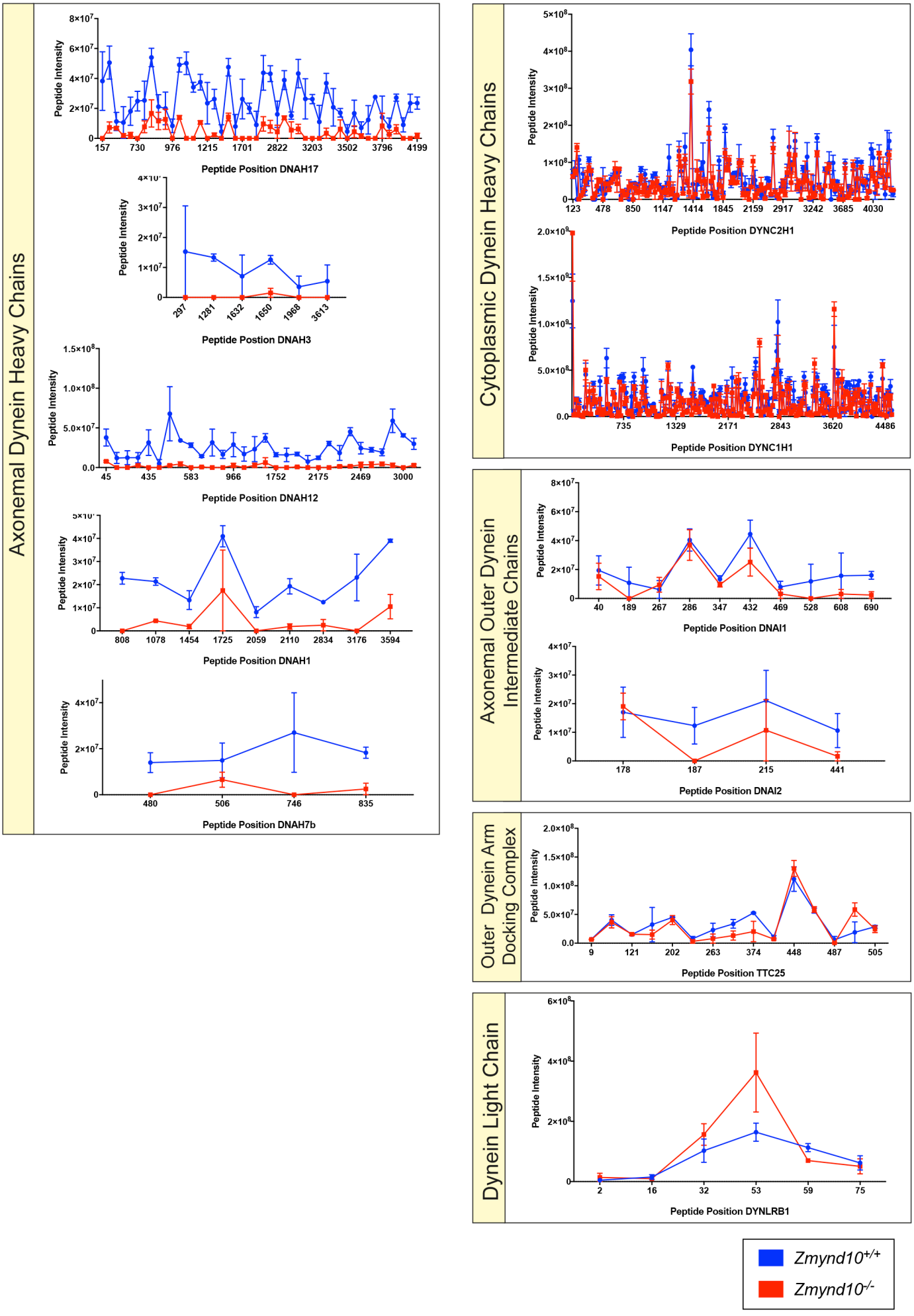
Axonemal Dynein Heavy Chains
Peptide Intensity
Peptide Position DNAH17
Peptide Postion DNAH3
Peptide Position DNAH12
Peptide Position DNAH1
Peptide Position DNAH7b
Cytoplasmic Dynein Heavy Chains
Peptide Position DYNC2H1
Peptide Position DYNC1H1
Axonemal Outer Dynein Intermediate Chains
Peptide Position DNAI1
Peptide Position DNAI2
Outer Dynein Arm Docking Complex
Peptide Position TTC25
Dynein Light Chain
Peptide Position DYNLRB1
Zmynd10+/+
Zmynd10-/-

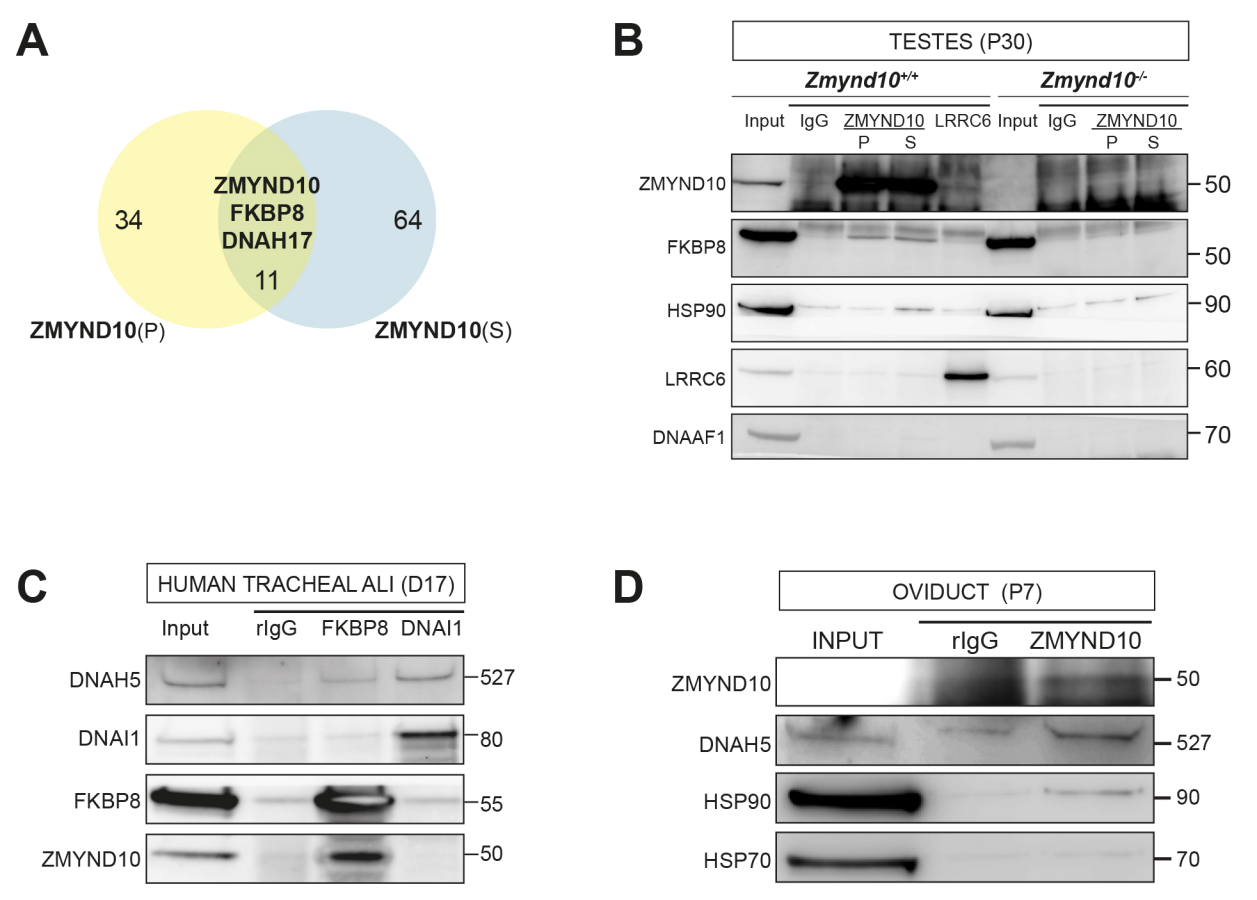
A
34
ZMYND10
FKBP8
DNAH17
11
64
ZMYND10(P)
ZMYND10(S)
B
TESTES (P30)
Zmynd10+/+
Zmynd10-/-
Input
IgG
ZMYND10
P
S
LRRC6
Input
IgG
ZMYND10
P
S
ZMYND10
FKBP8
HSP90
LRRC6
DNAAF1
50
50
90
60
70
C
HUMAN TRACHEAL ALI (D17)
Input
rIgG
FKBP8
DNAI1
DNAH5
DNAI1
FKBP8
ZMYND10
527
80
55
50
D
OVIDUCT (P7)
INPUT
rIgG
ZMYND10
ZMYND10
DNAH5
HSP90
HSP70
50
527
90
70

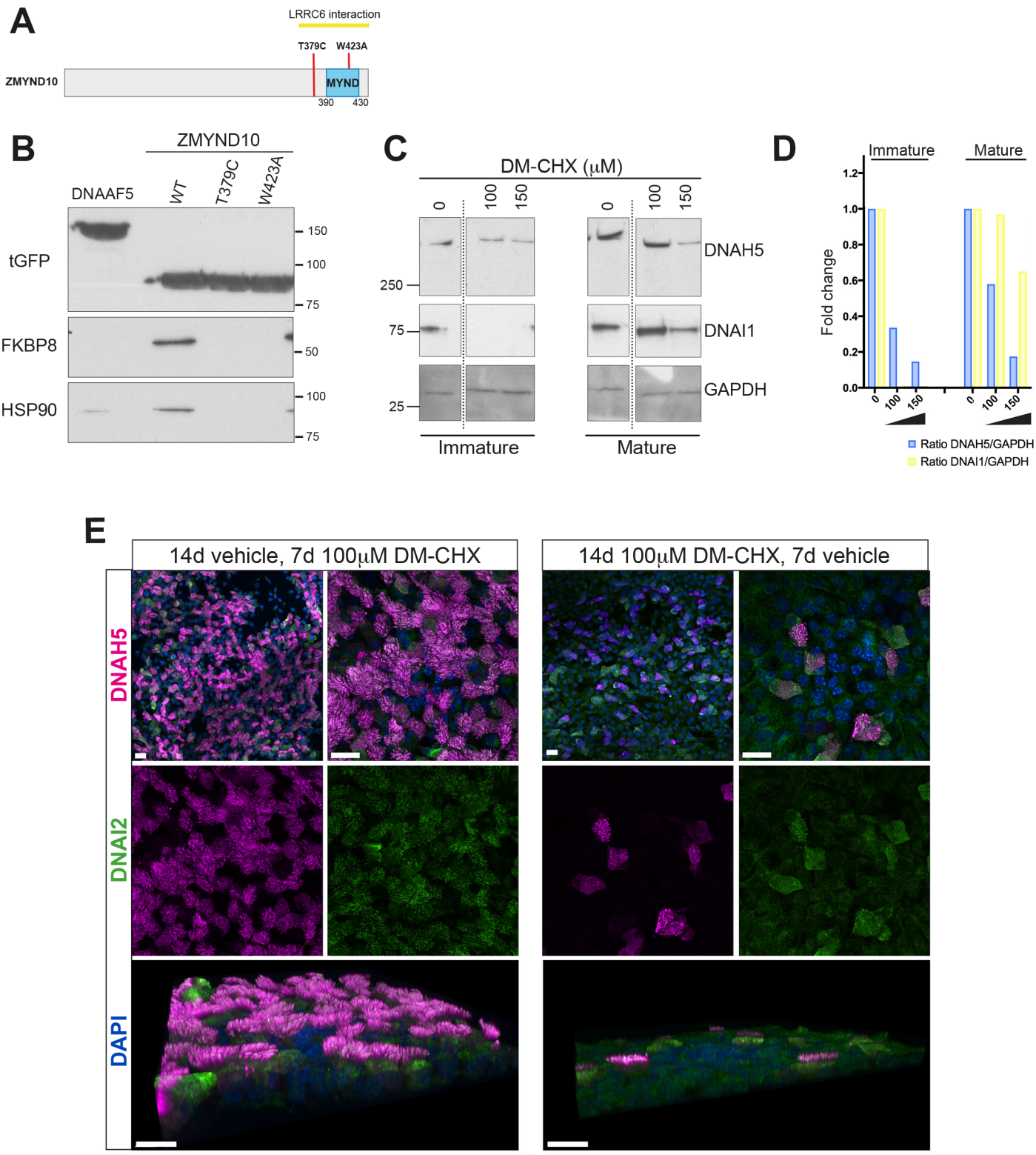
A
LRRC6 interaction
T379C
W423A
ZMYND10
MYND
390
430
B
ZMYND10
DNAAF5
WT
T379C
W423A
tGFP
FKBP8
HSP90
150
100
75
50
100
75
C
DM-CHX (μM)
0
100
150
0
100
150
250
75
25
DNAH5
DNAI1
GAPDH
Immature
Mature
D
Immature
Mature
Fold change
1.2
1.0
0.8
0.6
0.4
0.2
0.0
0
100
150
0
100
150
Ratio DNAH5/GAPDH
Ratio DNAI1/GAPDH
E
14d vehicle, 7d 100μM DM-CHX
14d 100μM DM-CHX, 7d vehicle
DNAH5
DNAI2
DAPI

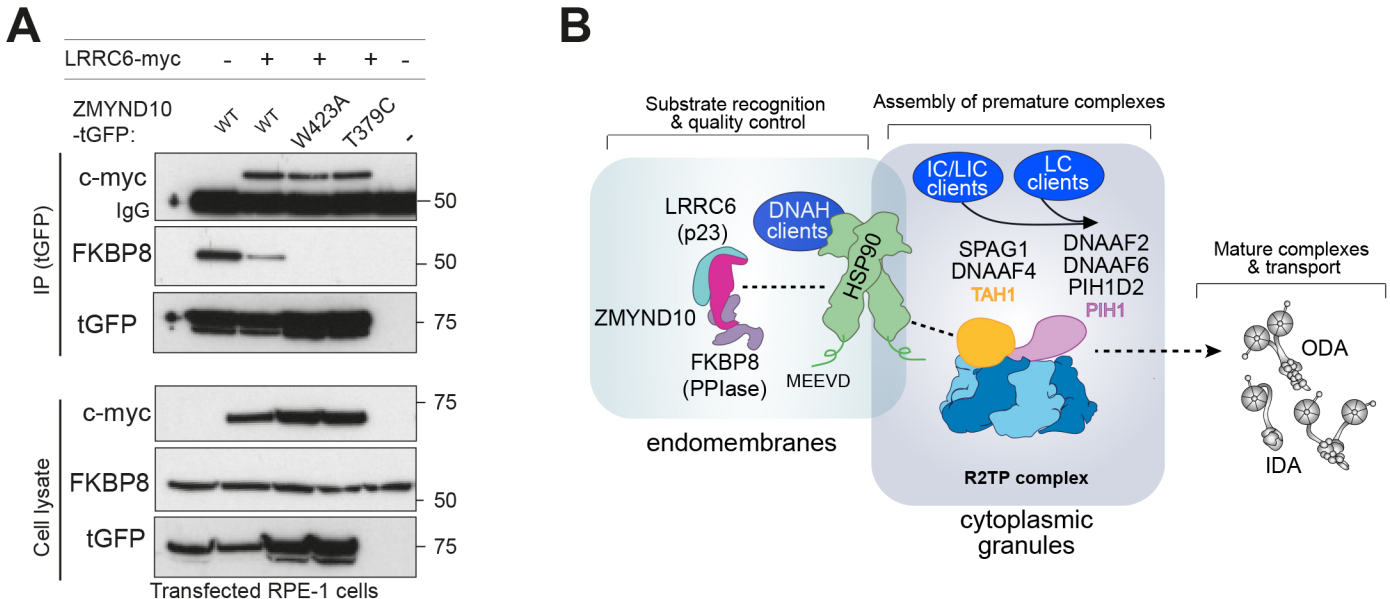
A
LRRC6-myc - + + + -
ZMYND10 -tGFP:
WT
WT
W423A
T379C
-
IP (tGFP)
c-myc
IgG
FKBP8
tGFP
50
50
75
Cell lysate
c-myc
FKBP8
tGFP
75
50
75
Transfected RPE-1 cells
B
Substrate recognition & quality control
Assembly of premature complexes
LRRC6 (p23)
DNAH clients
HSP90
ZMYND10
FKBP8 (PPIase)
MEEVD
endomembranes
IC/LIC clients
LC clients
SPAG1
DNAAF4
TAH1
DNAAF2
DNAAF6
PIH1D2
PIH1
R2TP complex
cytoplasmic granules
Mature complexes & transport
ODA
IDA